

# Modeling global carbon and water fluxes and hyperspectral canopy radiative transfer simultaneously using a next generation land surface model—CliMA Land

Yujie Wang<sup>1</sup>, Renato Kerches Braghieri<sup>2</sup>, Marcos Longo<sup>2</sup>, Alexander Norton<sup>3</sup>, Philipp Köhler<sup>1</sup>, Russell Doughty<sup>1</sup>, Yi Yin<sup>1</sup>, A. Anthony Bloom<sup>4</sup>, and Christian Frankenberg<sup>1</sup>

<sup>1</sup>California Institute of Technology

<sup>2</sup>NASA Jet Propulsion Laboratory

<sup>3</sup>Unknown

<sup>4</sup>Jet Propulsion Laboratory, California Institute of Technology

November 24, 2022

## Abstract

Recent progress in satellite observations has provided unprecedented opportunities to monitor vegetation activity on the global scale. However, a major challenge in fully utilizing remotely sensed data to constrain land surface models (LSMs) lies in inconsistencies between simulated and observed quantities. Transpiration and gross primary productivity (GPP) that traditional LSMs simulate are not directly measurable from space and they are inferred from spaceborne observations using assumptions that are inconsistent with those of the LSMs, whereas canopy reflectance and fluorescence spectra that satellites can detect are not modeled by traditional LSMs. To bridge these quantities, we present the land model developed within the Climate Modeling Alliance (CliMA), which simulates global-scale GPP, transpiration, and hyperspectral canopy radiative transfer (RT). Thus, CliMA Land can predict any vegetation index or outgoing radiance, including solar-induced chlorophyll fluorescence (SIF), normalized difference vegetation index (NDVI), enhanced vegetation index (EVI), and near infrared reflectance of vegetation (NIRv) for any given measurement geometry. Even without parameter optimization, the modeled spatial patterns of CliMA Land GPP, SIF, NDVI, EVI, and NIRv correlate significantly with existing observational products. CliMA Land is also very useful in its high temporal resolution, e.g., providing insights into when GPP, SIF, and NIRv diverge. Based on comparisons between models and observations, we propose ways to improve future land modeling regarding data processing and model development.

# Modeling global carbon and water fluxes and hyperspectral canopy radiative transfer simultaneously using a next generation land surface model—CliMA Land

Y. Wang<sup>1</sup>, R. K. Braghieri<sup>2,3</sup>, M. Longo<sup>2,4</sup>, A. J. Norton<sup>2</sup>, P. Köhler<sup>1</sup>, R. Doughty<sup>1,5</sup>, Y. Yin<sup>1</sup>, A. A. Bloom<sup>2</sup>, and C. Frankenberg<sup>1,2</sup>

<sup>1</sup>Division of Geological and Planetary Sciences, California Institute of Technology, Pasadena, California 91125, USA

<sup>2</sup>Jet Propulsion Laboratory, California Institute of Technology, Pasadena, California 91109, USA

<sup>3</sup>Joint Institute for Regional Earth System Science and Engineering, University of California at Los Angeles, Los Angeles, California 90095, USA

<sup>4</sup>Climate and Ecosystem Sciences Division, Lawrence Berkeley National Laboratory, Berkeley, California 94720, USA

<sup>5</sup>College of Atmospheric & Geographic Sciences, GeoCarb Mission, University of Oklahoma, Norman, Oklahoma 73019, USA

## Key Points:

- Hourly carbon and water fluxes, and hyperspectral canopy radiative transfer are simulated simultaneously
- Modeled indices well capture the spatial patterns across the globe
- The model highlights need and possibility of fusing data from multiple sources

---

Corresponding author: Y. Wang, [wujie@caltech.edu](mailto:wujie@caltech.edu)

Corresponding author: A. A. Bloom, [alexis.a.bloom@jpl.nasa.gov](mailto:alexis.a.bloom@jpl.nasa.gov)

Corresponding author: C. Frankenberg, [cfranken@caltech.edu](mailto:cfranken@caltech.edu)

**Abstract**

Recent progress in satellite observations has provided unprecedented opportunities to monitor vegetation activity on the global scale. However, a major challenge in fully utilizing remotely sensed data to constrain land surface models (LSMs) lies in inconsistencies between simulated and observed quantities. Transpiration and gross primary productivity (GPP) that traditional LSMs simulate are not directly measurable from space and they are inferred from spaceborne observations using assumptions that are inconsistent with those of the LSMs, whereas canopy reflectance and fluorescence spectra that satellites can detect are not modeled by traditional LSMs. To bridge these quantities, we present the land model developed within the Climate Modeling Alliance (CliMA), which simulates global-scale GPP, transpiration, and hyperspectral canopy radiative transfer (RT). Thus, CliMA Land can predict any vegetation index or outgoing radiance, including solar-induced chlorophyll fluorescence (SIF), normalized difference vegetation index (NDVI), enhanced vegetation index (EVI), and near infrared reflectance of vegetation (NIRv) for any given measurement geometry. Even without parameter optimization, the modeled spatial patterns of CliMA Land GPP, SIF, NDVI, EVI, and NIRv correlate significantly with existing observational products. CliMA Land is also very useful in its high temporal resolution, e.g., providing insights into when GPP, SIF, and NIRv diverge. Based on comparisons between models and observations, we propose ways to improve future land modeling regarding data processing and model development.

**Plain Language Summary**

The land is a big sink of CO<sub>2</sub>, but there is not a direct way to measure its carbon sink strength at the global scale. Researchers often use eddy covariance flux tower and/or satellite observations to infer land carbon sink strength. However, the flux towers are too sparsely distributed, and satellites can only detect radiation-related properties of the vegetation such as solar induced chlorophyll fluorescence. We bridge the two aspects by developing a new land surface model that simultaneously simulates both carbon and water fluxes as well as spectrally resolved canopy radiation properties. We compare our model outputs directly to not only carbon flux estimations but also satellite observations. We show that our new land surface model can represent how carbon flux and canopy radiation properties vary across the globe and help understand

52 how ecosystems work under different environmental conditions. We believe advances  
53 in data processing and implementation of new features in land modeling will improve  
54 the land surface model predictive skills in the future.

## 55 **1 Introduction**

56 The land system sequesters approximately 25% of anthropogenic CO<sub>2</sub> emissions  
57 (Le Quéré et al., 2018), which slows the increase of atmospheric CO<sub>2</sub> concentration and  
58 thus global climate change. However, it is highly uncertain how the strength of  
59 terrestrial carbon sink will change in the future given that warmer global temperatures  
60 impact vegetation carbon fixation in diverging ways and that higher CO<sub>2</sub> concentration  
61 fertilizes leaf photosynthesis (Sperry et al., 2019). Despite the importance of the  
62 magnitude of land net CO<sub>2</sub> uptake, overall spatial and temporal global terrestrial  
63 carbon sink strength patterns remain poorly understood given the lack of direct  
64 observations at the landscape scale globally. As a result, the estimation of the global  
65 terrestrial carbon sink is largely dependent on data interpolation and/or modeling.

66 Gross primary productivity (GPP) is the most direct measure of the gross land  
67 carbon sink. However, global scale GPP products from various studies differ  
68 dramatically (Anav et al., 2015) due to differences in (i) the model selection, such as  
69 stomatal model parameters (Medlyn, Duursma, & Zeppel, 2011), soil moisture response  
70 (Powell et al., 2013; Trugman et al., 2018), and canopy structure setup (Braghiere et al.,  
71 2019, 2020; Y. Wang & Frankenberg, 2021), and (ii) the major drivers used to force the  
72 model, such as flux tower data (e.g., Jung et al., 2011; Tramontana et al., 2016; Jung et  
73 al., 2020) or remote sensing data (e.g., Zhang et al., 2017). Furthermore, the rapidly  
74 changing climate and increasing atmospheric CO<sub>2</sub> make it more challenging for the  
75 models to agree on the magnitude and direction of the future land carbon sink  
76 strength (Anav et al., 2013; Arora et al., 2013; Jones et al., 2013; Anav et al., 2015; Zhang  
77 & Ye, 2021).

78 GPP divergence caused by model selection may be considered as a result of the  
79 various forms of forcing data. For example, eddy covariance flux towers provide  
80 relatively high quality half-hourly carbon and water fluxes (Baldocchi et al., 2001;  
81 Baldocchi, 2020), but are too sparsely distributed, and modeler have to rely on data  
82 interpolation for global interpretation. Also, GPP is not directly measured but

83 partitioned from ecosystem net carbon flux using nighttime flux measurements to  
84 proxy respiration rates, and this partitioning could result in biased GPP estimates  
85 (Wehr et al., 2016). In comparison, spaceborne remote sensing data provide good  
86 spatial coverage (Schimel et al., 2015, 2019), but often have coarse temporal resolution  
87 and cannot directly measure carbon or water fluxes. Models based on remote sensing  
88 often have to rely on empirically correlating GPP with various quantities based on  
89 reflectance and/or fluorescence. As a result, a satisfactory approach to parameterize  
90 land surface models (LSMs) consistently at the global scale is lacking, and  
91 model-observation comparisons are inconsistent. In theory, if the LSMs can correctly  
92 account for vegetation processes and are given the same high quality flux and climate  
93 forcing data, these models should be able to predict similar GPP once their model  
94 parameters (e.g., leaf area index, plant functional type distributions, leaf photosynthetic  
95 capacity, and plant hydraulic traits) are optimized for the input training data.  
96 Currently, high quality carbon and water flux data are sparse, which makes model  
97 parameterization and development challenging and hence their GPP predictions are  
98 unreliable. Therefore, a key step for improving land modeling is to integrate data from  
99 multiple sources, equip LSMs with corresponding features to simulate observations,  
100 and parameterize the LSMs by minimizing the model-data mismatch.

101 Remotely sensed data that are useful to constrain land processes at regional and  
102 global scales are mostly based on observed reflected and emitted radiances and optical  
103 depths of vegetation canopies (e.g., Badgley et al., 2017; Sun et al., 2017; Konings et al.,  
104 2021). Among the various index and radiance measures, solar-induced chlorophyll  
105 fluorescence (SIF) and near infrared reflectance of vegetation (NIRv) are the two most  
106 promising candidates for estimating GPP given their overall good correlations with  
107 GPP (Frankenberg et al., 2011; Badgley et al., 2017; Sun et al., 2018; Badgley et al., 2019;  
108 Doughty et al., 2021). Nevertheless, the intermediate step of translating SIF and/or  
109 NIRv to GPP may introduce additional biases given the decoupled correlations among  
110 them in light saturated environments (Zhang et al., 2016), drought stressed conditions  
111 (Helm et al., 2020), cold winters (Magney et al., 2019), and over diversely structured  
112 vegetation (Braghiere et al., 2021).

113 Alternatively, a better way to utilize the remote sensing data would be to match  
114 modeled canopy fluorescence and reflectance spectra to satellite retrievals directly  
115 (Norton et al., 2018; Shiklomanov et al., 2021; Y. Wang, Köhler, et al., 2021). This,

116 however, requires LSMs to move from simple broadband canopy radiative transfer (RT)  
117 to a hyperspectral canopy RT in order to utilize spectrally resolved remote sensing data  
118 (e.g., Norton et al., 2019), which most existing LSMs are not designed to do. We note  
119 that traditional LSMs can be extended to utilize satellite data through scaling leaf level  
120 SIF up to canopy level using two leaf radiation scheme (e.g., Qiu et al., 2019). However,  
121 this empirical approach discards useful information that the hyperspectral and  
122 multi-layer approach contains, such as the sun-sensor geometry and vertical canopy  
123 gradients in fluorescence and photosynthesis yields, which interact non-linearly.

124 Our recent efforts bridge land modeling and observations together in a new LSM  
125 as part of a new generation earth system model within the Climate Modeling Alliance,  
126 CliMA (<https://clima.caltech.edu>; Y. Wang, Köhler, et al., 2021). The new model  
127 can simulate hyperspectral canopy RT in a multi-layer canopy, enabling us to  
128 simultaneously simulate canopy carbon and water fluxes as well as corresponding  
129 canopy fluorescence and reflectance spectra. Our new LSM, CliMA Land, improves the  
130 representation of SIF at the canopy scale (Braghiere et al., 2021) and well captures the  
131 carbon and water fluxes measured at flux tower sites (Y. Wang, Köhler, et al., 2021). In  
132 particular, the simultaneously simulated GPP, SIF, and NIRv allow for many potential  
133 studies that are not possible in the past, say the diurnal cycles and correlations among  
134 SIF, NIRv, and GPP at various temporal resolutions.

135 In this study, we (i) describe the general model framework of CliMA Land, (ii)  
136 detail the model parameterization and simulation procedure, and (iii) show our first  
137 global run using CliMA Land, the first LSM that outputs hourly canopy fluorescence  
138 and reflectance spectra along with corresponding carbon and water fluxes. In section 3,  
139 we investigate how well CliMA Land GPP, SIF, and other reflectance indices capture  
140 their spatial patterns. We run our model for the years 2010 and 2019, and compare our  
141 model outputs with flux tower observation-based datasets for the year 2010 and with  
142 other satellite-based GPP and SIF products for the year 2019. Finally, we discuss  
143 potential ways to improve future land modeling using the new LSM framework.

## 144 **2 Materials and Methods**

145 To facilitate research with various scales and model selections, CliMA Land is  
146 highly modular, containing plant hydraulics, stomatal control, canopy RT, and

147 soil-plant-air continuum sub-modules, each of which can be used as a standalone  
 148 package (Figure 1; Y. Wang, Köhler, et al., 2021; Y. Wang & Frankenberg, 2021).  
 149 Through simulating hyperspectral canopy RT and scaling leaf level gas exchange, we  
 150 can integrate total canopy carbon and water fluxes, and simulate a number of remotely  
 151 sensible quantities (such as SIF and NIRv) simultaneously at arbitrarily fine time steps  
 152 at the global scale (here for the Nadir viewing satellite direction). CliMA Land code  
 153 and documentation are publicly and freely available at  
 154 <https://github.com/CliMA/Land> (the exact version of model is archived at Y. Wang,  
 155 Braghieri, & Frankenberh, 2021, last access: 15 Nov 2021). Below, we describe the  
 156 general CliMA Land framework and the procedure we used for the global simulations.

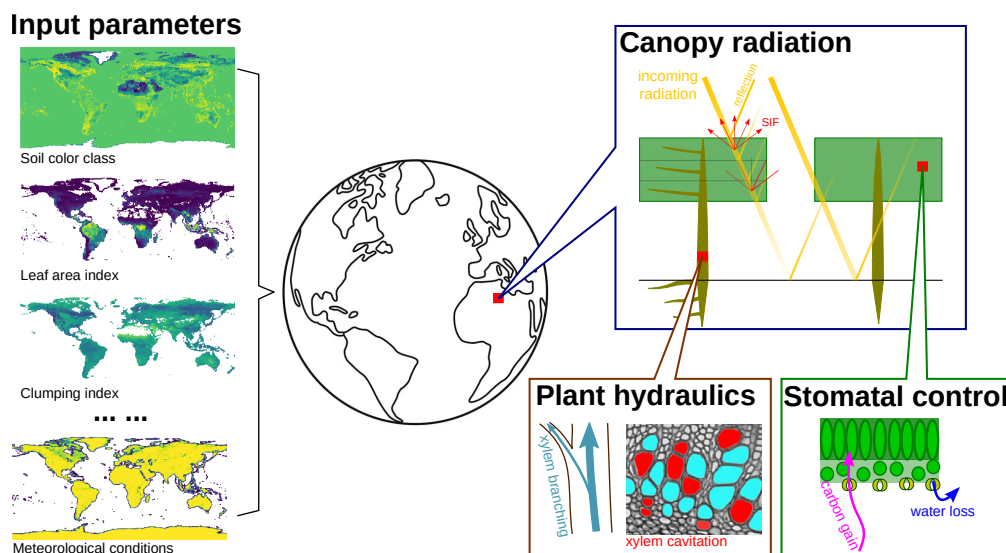


**Figure 1.** Diagram of the model framework and parameterization of CliMA Land. CliMA Land consists of three key modules: canopy radiative transfer (RT), plant hydraulics, and stomatal control. Canopy RT module is responsible for canopy RT simulation; plant hydraulic module accounts for the water movement from soil to the air; stomatal control module addresses the leaf gas exchange. To run CliMA Land at the global scale, various input parameters are used to initialize the site such as soil color class, leaf area index, clumping index, and meteorological conditions. Then each site is treated as a bulk forest with bulk plant traits, and carbon and water fluxes and canopy spectra are simulated using the soil-plant-air continuum model.

## 2.1 CliMA Land

CliMA Land (v0.1; Y. Wang, Köhler, et al., 2021) considers a grid cell (e.g., a  $1^\circ \times 1^\circ$  grid) as a “mono-species” stand in which all plants have the same size with a suite of bulk properties (such as canopy height, clumping index, and leaf chlorophyll content; Figure 1). CliMA Land supports freely customized plant hydraulic system ranging from a single organ (e.g., leaf, stem, or root) to a whole plant (such as grass and tree). CliMA Land also features a variety of stomatal models from empirical approaches (e.g., Ball et al., 1987; Medlyn, Duursma, Eamus, et al., 2011) to stomatal optimization theories (e.g., Sperry et al., 2017; Y. Wang et al., 2020). Further, CliMA Land can simulate canopy RT using either the traditional two leaf RT approach by partitioning the canopy to sunlit and shaded fractions with broadband radiative transfer scheme (Campbell & Norman, 1998), or a more complex multi-layer canopy model that accounts for hyperspectral radiation, leaf angular distribution and canopy clumping (Yang et al., 2017; Braghieri et al., 2021; Y. Wang, Köhler, et al., 2021; Yang et al., 2021).

### 2.1.1 Plant Hydraulic Architecture

Plant hydraulics in CliMA Land is simulated numerically by partitioning the plant into root, stem, and leaf organs (Sperry & Love, 2015; Sperry et al., 2016), and a specific xylem vulnerability curve is used for each organ (the curve is allowed to differ within and among organs). The organs can be aligned in a flexible way (Y. Wang, Köhler, et al., 2021). For example, a tree comprises a multi-layer root system, a trunk (stem), a multi-layer canopy system (stem and leaf in series in each layer); a grass comprises a multi-layer root system and a multi-layer canopy system (only leaf is present in each layer). Further, the plant hydraulics sub-module allows for customizing root and stem height change, and thus is able to account for a gravitational pressure drop in the xylem (Y. Wang, Köhler, et al., 2021). Moreover, there is a drought legacy variable in each hydraulic organ (the xylem remembers the minimal xylem pressure and thus minimal hydraulic conductance it has experienced, and xylem hydraulic conductance is not allowed to be higher than this memory conductance due to irreversible xylem cavitation), and addressing this gives more realistic stomatal response to the environment after a drought (W. R. L. Anderegg et al., 2015; Y. Wang et al., 2020). We also account for temperature effects on water viscosity and surface

189 tension in our model, which could otherwise result in non-negligible simulated water  
190 transport biases (e.g., 1 °C difference in water temperature potentially results in c. 2.4%  
191 change in maximum hydraulic conductance; Reid et al., 1987).

192 Plant hydraulic architecture may impact the stomatal models in CliMA Land  
193 (not always as some stomatal models do not rely on plant hydraulics at all, see  
194 examples in section 2.1.2). With the ascent of sap along the xylem, xylem water  
195 pressure typically gets more and more negative, potentially resulting in xylem  
196 cavitation. The higher the water flux in the xylem and/or the drier the soil, the higher  
197 the risk of xylem cavitation. Loss of plant water transport capability may harm plants'  
198 leaf gas exchange performance given the limited water supply to leaves, and thus  
199 plants may regulate their stomata to alleviate the risk (Sperry & Love, 2015).  
200 Combining photosynthetic carbon gain and hydraulic risk leads to a variety of stomatal  
201 optimization models that simulate stomatal behavior using plant traits rather than  
202 empirically fitted parameters (see Y. Wang et al. (2020) for an overview). Furthermore,  
203 plant hydraulic status is also used in more and more empirical stomatal models (e.g.,  
204 Kennedy et al., 2019), acting as a tuning factor to link stomatal responses to soil  
205 moisture status.

### 206 **2.1.2 Stomatal Control**

207 Stomatal behavior in CliMA Land can be simulated using either empirical  
208 models that rely on statistically fitted parameters or stomatal optimization models that  
209 are based on plant traits and processes. To date, CliMA Land embeds three published  
210 empirical stomatal models, namely the Ball et al. (1987), Leuning (1995), and Medlyn,  
211 Duursma, Eamus, et al. (2011) models. These empirical models can be used along with  
212 two general types of tuning factors to force stomatal response to drought, one of which  
213 takes effect through tuning the empirical model parameters (such as the slope  
214 parameter  $g_1$ ) and another takes effect via down-regulating photosynthetic capacity  
215 (e.g., Kennedy et al., 2019). CliMA Land also supports four published stomatal  
216 optimization models based on plant hydraulics given their best performance in three  
217 datasets (W. R. Anderegg et al., 2018; Venturas et al., 2018; Y. Wang et al., 2019), and  
218 they are Sperry et al. (2017), W. R. Anderegg et al. (2018), Eller et al. (2018), and  
219 Y. Wang et al. (2020) models. These optimization based models are less dependent on  
220 fitting parameters and performed well compared to empirical models, though are more

221 difficult to parameterize. Further, the optimization framework can be extended to  
222 account for nighttime transpiration responses to the environment (Y. Wang, Anderegg,  
223 et al., 2021), showing great potential in advancing land surface modeling.

224 Despite the predictive skills of optimization models in predicting stomatal  
225 responses to the environment, particularly soil moisture, difficulties in parameterizing  
226 these models hamper the use of trait- and optimization-based stomatal models at global  
227 scales. As a result, empirical models are still the top candidates for land surface models  
228 before reliable spatially resolved hydraulic trait maps become available. Similarly,  
229 tuning empirical model parameter  $g_1$  or photosynthetic capacity based on plant  
230 hydraulics does not work either. For example, D. M. Lawrence et al. (2019) and  
231 Kennedy et al. (2019) proposed to use hydraulic conductance to tune leaf  
232 photosynthetic capacity; however, the calculation of hydraulic conductance relies on the  
233 xylem vulnerability curve as well as whole plant hydraulic conductance, which are  
234 spatially unknown at global scales at present. Thus, to date, simulating global land  
235 carbon and water fluxes is still limited to empirical models and tuning factors based on  
236 soil conditions rather than plant hydraulics. However, with CliMA Land, we provide  
237 more alternatives that can be used in the future when globally spatial hydraulic trait  
238 maps become available or can be inferred using, for instance, evapotranspiration  
239 measurements or skin temperature in general.

### 240 *2.1.3 Canopy Radiative Transfer*

241 CliMA Land features two possible canopy RT schemes: single layered two leaf  
242 RT model with sunlit and shaded fractions simulating broadband reflectance and  
243 transmittance (Campbell & Norman, 1998), and a vertically layered canopy model with  
244 leaf angular distribution simulating hyperspectral reflectance and transmittance  
245 (adapted from Soil Canopy Observation of Photosynthesis and Energy fluxes model,  
246 SCOPE van der Tol et al., 2009; Yang et al., 2017). While the inclusion of the two leaf  
247 canopy RT model allows for compatibility with other vegetation models, the use of a  
248 complex multi-layer canopy model enables the simulation of canopy reflectance and  
249 fluorescence as well as carbon and water fluxes simultaneously, promoting the  
250 integration of land models with remote sensing observations (Y. Wang, Köhler, et al.,  
251 2021). Moreover, the multi-layer canopy model also supports vertically resolved  
252 heterogeneous micro-climates and leaf physiology within the canopy (Bonan et al.,

253 2018, 2021; Y. Wang & Frankenberg, 2021). Future research aiming to quantitatively  
 254 understand the vertical canopy layout (such as optimal nutrient and leaf area  
 255 partitioning) will further improve the predictive skills of the land surface models.

256 Compared to the original SCOPE canopy RT scheme, (1) we implemented a  
 257 clumping index in CliMA Land to account for the horizontal heterogeneity in the  
 258 canopy (Pinty et al., 2006; Braghieri et al., 2019, 2020). The inclusion of a clumping  
 259 index can promote light scattering into lower canopy layers, and improves model  
 260 predictive skills against benchmark 3D datasets (Braghiere et al., 2021). (2) We  
 261 accounted for carotenoid absorption as absorbed photosynthetically active radiation by  
 262 the antenna systems, thus photosynthesis and chlorophyll fluorescence (Y. Wang,  
 263 Köhler, et al., 2021). (3) We converted energy flux to photon flux and computed SIF in  
 264 terms of photon (to use with fluorescence quantum yield); and then we convert SIF  
 265 photon flux back to energy flux in the SIF radiative transfer (Y. Wang & Frankenberg,  
 266 2021). (4) In the present study, we further expand the soil albedo implementation to  
 267 hyperspectral simulations to make land modeling more realistic in terms of canopy RT  
 268 and gas exchange simulations. In brief, soil albedo values at photosynthetically active  
 269 radiation (PAR) region and near infrared (NIR) regions, denoted as  $\alpha_{\text{PAR}}$  and  $\alpha_{\text{NIR}}$   
 270 respectively, are calculated by linearly interpolating the reference values at completely  
 271 wet and dry soils (see Note S1 for more details):

$$272 \quad \alpha_{\text{PAR}} = \alpha_{\text{PAR,wet}} \cdot \text{RSWC} + \alpha_{\text{PAR,dry}} \cdot (1 - \text{RSWC}), \quad (1)$$

$$273 \quad \alpha_{\text{NIR}} = \alpha_{\text{NIR,wet}} \cdot \text{RSWC} + \alpha_{\text{NIR,dry}} \cdot (1 - \text{RSWC}), \quad (2)$$

274 where RSWC is the relative volumetric soil water content (0 when completely dry, 1  
 275 when soil water content is saturated), the subscript “wet” denotes saturated soil, and  
 276 the subscript “dry” denotes completely dry soil.

## 277 **2.2 Model Parameterization**

### 278 **2.2.1 Soil and Air**

279 Soil color impacts soil albedo calculations and thus canopy RT and gas exchange.  
 280 We used the Community Land Model soil color class map (data from P. J. Lawrence &  
 281 Chase, 2007) and soil albedo reference table (Table 3.3 in CLM5 tech notes) to describe  
 282 broadband soil albedo values at PAR and NIR regions. Note here that CliMA Land  
 283 supports using either broadband or hyperspectral soil albedo. When hyperspectral soil

284 albedo scheme was selected, we extrapolated the broadband  $\alpha_{\text{PAR}}$  and  $\alpha_{\text{NIR}}$  to a  
 285 hyperspectral spectrum by fitting the mean hyperspectral  $\alpha_{\text{PAR}}$  to broadband  $\alpha_{\text{PAR}}$  and  
 286 hyperspectral  $\alpha_{\text{NIR}}$  to a flat constant  $\alpha_{\text{NIR}}$  in the NIR region using the characteristic  
 287 curves from (Jiang & Fang, 2019) (see Note S1 for more details):

$$288 \min \left[ \left( \overline{\alpha_{\text{PAR,mod}}} - \alpha_{\text{PAR,ref}} \right)^2 + \left( \left| \alpha_{\text{NIR,mod}} - \alpha_{\text{NIR,ref}} \right| \right)^2 \right] \quad (3)$$

289 The same soil color class map was used for simulations at different years of global run.

290 Soil hydraulic parameters impact soil water stress to plants (and thus stomatal  
 291 and SIF responses to soil moisture). We used the van Genuchten equation to describe  
 292 soil hydraulic parameters (van Genuchten, 1980). We used gridded van Genuchten  
 293 parameters including soil retention curve characteristic parameters (soil air entry  
 294 suction and soil pore-size distribution), residual soil water content, and saturated soil  
 295 water content (data from Dai et al., 2019). The soil hydraulic dataset includes van  
 296 Genuchten parameters for 4 soil layers, with the layer boundaries range from a soil  
 297 depth from 0 to 0.1, 0.35, 1, and 3 m; and we partitioned plant root layering  
 298 accordingly to 4 layers. The same soil van Genuchten parameter map was used for  
 299 simulations at different years. Eventually, we will be able to use arbitrary vertical  
 300 resolutions and solve the Richard's equation in both 1D and 3D.

301 Atmospheric  $\text{CO}_2$  concentration impacts leaf level gas exchange and SIF  
 302 simulation. We used the annual mean  $\text{CO}_2$  concentration for each year regardless of  
 303 the spatial and temporal variations within a year (data from  
 304 <https://gml.noaa.gov/ccgg/trends/data.html>). A global mean  $\text{CO}_2$  concentration  
 305 was used for simulations at the specific year (e.g., 389 ppm in 2010, and 410 ppm in  
 306 year 2019).

307 Climate forcing impacts the plants' stomatal opening and photosynthesis  
 308 kinetics, and thus carbon and water fluxes as well as canopy reflectance and  
 309 fluorescence spectra. We downloaded hourly reanalysis weather data with  $0.25^\circ \times 0.25^\circ$   
 310 spatial resolution from the ERA5 data portal (Hersbach et al., 2018, 2020), and used it  
 311 to force CliMA Land simulation, i.e. canopy temperature and humidity are currently  
 312 prescribed but will be dynamically coupled to the atmosphere in the future. The ERA5  
 313 reanalysis data we used included wind speed at 10 m (used to determine leaf  
 314 boundary layer thickness), dew point temperature and air temperature at 2 m (used to  
 315 compute atmospheric vapor pressure deficit), skin temperature (prescribed, used as a

316 proxy for leaf temperature), mean direct and total surface shortwave radiation (used to  
 317 compute direct and diffuse radiation to feed to canopy RT), surface atmosphere  
 318 pressure, and soil temperature and volumetric water content at four soil layers. Note  
 319 that the soil layering of ERA5 differs slightly from the soil hydraulic parameters in that  
 320 the layer boundaries of the ERA5 data range from 0 to 0.07, 0.28, 1, and 2.89 m, and we  
 321 used the van Genuchten parameters from the soil map in Dai et al. (2019) despite the  
 322 minor mismatch in soil depth profiles.

### 323 **2.2.2 Plant Traits**

324 As the pigments that absorb PAR in the antenna system, chlorophyll and  
 325 carotenoid contents impact leaf-level reflectance and transmittance, and canopy-level  
 326 radiative transfer and thus leaf gas exchange. We used weekly mean leaf chlorophyll  
 327 contents to represent seasonality of canopy greenness (data from Croft et al., 2020), and  
 328 assumed leaf carotenoid content being 1/7 of the chlorophyll content (Croft et al.,  
 329 2020). We note that the ratio between carotenoid and chlorophyll can be highly  
 330 variable, and future research into their spatial and temporal variability will make the  
 331 simulations more accurate. The weekly mean chlorophyll content was averaged from  
 332 values in the same week from multiple years, and thus the same leaf chlorophyll  
 333 content dataset was used for simulations at different years.

334 Leaf mass per area (LMA) impacts reflectance and transmittance of a leaf, and  
 335 canopy RT and hence leaf gas exchange. We used a globally gridded specific leaf area  
 336 (SLA = 1/LMA) in our global land model run (Butler et al., 2017). The same LMA  
 337 dataset was used for simulations at different years of global run.

338 Leaf photosynthetic capacity impacts leaf gas exchange and fluorescence  
 339 quantum yield. We used the leaf photosynthetic capacity (represented by maximum  
 340 carboxylation rate at a reference temperature of 25 °C— $V_{\text{cmax}25}$ ) from a recent machine  
 341 learning based product (Luo et al., 2021). The  $V_{\text{cmax}25}$  was assumed time-invariant.  
 342 Maximum electron transport rate at a reference temperature of 25 °C— $J_{\text{max}25}$  and  
 343 respiration rate at a reference temperature of 25 °C— $R_{\text{d}25}$  were scaled from  $V_{\text{cmax}25}$  in  
 344 that  $J_{\text{max}25} = 1.67 \cdot V_{\text{cmax}25}$  and  $R_{\text{d}25} = 0.015 \cdot V_{\text{cmax}25}$ , consistently with (Sperry et al.,  
 345 2017). We assumed constant  $J_{\text{max}25} : V_{\text{cmax}25}$  and  $R_{\text{d}25} : V_{\text{cmax}25}$  ratios due to the lack of  
 346 global datasets, however we note that there is evidence that they vary across the globe

347 (e.g., Walker et al., 2014; Norby et al., 2017). The same photosynthetic capacity dataset  
348 was used for simulations at different years.

349 Leaf area index (LAI) impacts canopy RT and whole plant gas exchange. We  
350 used the gridded Moderate Resolution Imaging Spectroradiometer (MODIS) LAI  
351 product at  $0.5^\circ \times 0.5^\circ$  spatial resolution and 8-day temporal resolution (data from Yuan  
352 et al., 2020). See Yuan et al. (2011) for more details of the LAI data quality control and  
353 gap filling. A time-dependent LAI was used in the simulations at the specific year  
354 years (e.g., LAI time series at year 2010 was used for the global simulation at year  
355 2010).

356 Canopy height impacts plant hydraulic architecture and thus leaf gas exchange.  
357 We used a globally resolved canopy height map to initialize plant hydraulic  
358 architecture within each simulated grid (Simard et al., 2011). If average plant height  
359 within the simulated grid was higher than 2 m, we treated the bulk plant as a tree  
360 (gravitational pressure drop was accounted for in the stem xylem); otherwise, we  
361 treated the bulk plant as a grass (gravitational pressure drop was ignored in the stem  
362 xylem). The same canopy height dataset was used for simulations at different years.

363 The clumping index impacts canopy RT and thus leaf gas exchange. We used a  
364 globally gridded clumping index to describe the horizontal canopy heterogeneity for  
365 each simulated grid (a constant clumping index for each pixel that does not change  
366 within and among growing seasons; He et al., 2012). The same canopy clumping index  
367 dataset was used for simulations in different years.

### 368 **2.2.3 Land Masks**

369 Stand elevation impacts atmospheric pressure, and thus leaf gas exchange. We  
370 used the elevation map from (Yamazaki et al., 2017) to initialize the land model at  
371 different grids.

372 Percentage of land in a grid impacts the scaled fluxes in a grid. We used the  
373 land-sea mask at  $0.25^\circ \times 0.25^\circ$  resolution from ERA5 reanalysis data (Hersbach et al.,  
374 2018).

375 The plant functional type (PFT) distribution impacts bulk properties of a site  
376 (such as the empirical slope parameter  $g_1$ ), and thus stomatal responses to the

377 environment. We used the CLM PFT distribution map (P. J. Lawrence & Chase, 2007)  
 378 to derive the empirical parameter  $g_1$  at each grid cell. For each grid, we calculated the  
 379 weighted  $g_1$  based on the PFT distribution ( $g_1$  for each PFT from De Kauwe et al.,  
 380 2015). The same PFT distribution map was used for simulations at different years in  
 381 the present study.

### 382 2.3 Global Simulations

383 We ran CliMA Land globally at  $1^\circ \times 1^\circ$  spatial resolution and an hourly temporal  
 384 resolution. We partitioned the Earth into 360 (in longitude)  $\times$  180 (in latitude) grids,  
 385 and regrided the model parameters spatially by averaging all the data that fell into  
 386 the target grid. For each pixel, we read data from the regrided model inputs as in  
 387 section 2.2, and performed the annual simulation if (1) none of the input data was  
 388 missing and (2) the pixel was vegetated. A total of 11288 grids were identified after  
 389 applying these filtering criteria.

390 For each grid, at each time step, we computed soil water potential for each soil  
 391 layer ( $\Psi_i$ ), and the tuning factor using  $\frac{\Psi_{\max} - \Psi_i}{\Psi_{\max} - \Psi_{\min}}$  for each soil layer ( $\Psi_{\max} = 0$  MPa,  
 392 and  $\Psi_{\min} = -5$  MPa by default). Then, we averaged the tuning factor for all soil layers,  
 393 and used it along with the  $g_1$  parameter of the Medlyn, Duursma, Eamus, et al. (2011)  
 394 model to simulate stomatal conductance. We did not use stomatal optimization models  
 395 in the present study because of the lack of global plant hydraulic trait maps. We ran  
 396 CliMA Land at steady state, and saved the model predicted hourly GPP, transpiration,  
 397 SIF at 683/740/757/771 nm (SIF<sub>683</sub>, SIF<sub>740</sub>, SIF<sub>757</sub>, and SIF<sub>771</sub>, respectively), normalized  
 398 difference vegetation index (NDVI), enhanced vegetation index (EVI), and NIRv  
 399 (Badgley et al., 2017):

$$400 \quad \text{NDVI} = \frac{\alpha_{\text{NIR}} - \alpha_{\text{RED}}}{\alpha_{\text{NIR}} + \alpha_{\text{RED}}}, \quad (4)$$

$$401 \quad \text{EVI} = 2.5 \cdot \frac{\alpha_{\text{NIR}} - \alpha_{\text{RED}}}{\alpha_{\text{NIR}} + 6 \cdot \alpha_{\text{RED}} - 7.5 \cdot \alpha_{\text{BLUE}} + 1}, \quad (5)$$

$$402 \quad \text{NIRv} = \text{NDVI} \cdot \alpha_{\text{NIR}}, \quad (6)$$

403 where  $\alpha$  is the albedo at the given wavelength (BLUE: 469 nm, RED: 645 nm, and NIR:  
 404 858.5 nm). We ran the simulations for the years 2010 and 2019.

## 2.4 Benchmarks

### 2.4.1 GPP

We compared CliMA Land predicted global GPP for year 2019 against the GPP product interpolated from flux tower using machine learning (MPI GPP; data from Tramontana et al., 2016). We selected and regridded the  $0.5^\circ \times 0.5^\circ$  MPI GPP at year 2019 that was based on (1) ensembles that include GPP and terrestrial ecosystem respiration from all flux partitioning methods, (2) ensembles that include carbon fluxes from all machine learning methods, and (3) all carbon fluxes from remote sensing, RS (RS GPP does not use meteorological forcing data). The data was labeled as “GPP.RS\_V006.FP-ALL.MLM-ALL.METEO-NONE” as noted at <https://www.fluxcom.org/CF-Download/>. It is worth noting that the MPI GPP is a machine-learning based upscaling of flux tower derived GPP (not true measurements), and that we compared CliMA GPP to this reference dataset rather than to flux tower derived GPP directly.

### 2.4.2 SIF

We compared CliMA Land predicted mean  $SIF_{683}$  and  $SIF_{740}$  to the daily average  $SIF_{683}$  and  $SIF_{740}$  retrieved using the TROPOspheric Monitoring Instrument, TROPOMI (data from Köhler et al., 2018; Doughty et al., 2021). We compare CliMA mean  $SIF_{757}$  and  $SIF_{771}$  to the daily average  $SIF_{757}$  and  $SIF_{771}$  retrieved using the Orbiting Carbon Observatory 2, OCO-2 (Sun et al., 2017). Note here that TROPOMI and OCO-2 SIF was averaged from observations with different sun-sensor geometry and that the day length correction was made with the assumption that SIF is function of the cosine of the solar zenith angle. In comparison, CliMA SIF was modeled at nadir direction (viewing zenith angle is  $0^\circ$ ), and the day length correction was made by averaging all modeled SIF at different times of a day.

### 2.4.3 NDVI, EVI, and NIRv

We compared CliMA Land predicted NDVI, EVI, and NIRv to those retrieved using the Moderate Resolution Imaging Spectroradiometer (MODIS) satellites MCD43A4 v006 dataset (Schaaf & Wang, 2015; Doughty et al., 2021). Note that MODIS MCD43A4 v006 reflectance indices have been corrected to nadir direction, which agrees

435 with CliMA Land simulations. We regridded the MODIS MCD43A4 v006 to global  
436 scale NDVI, EVI, and NIRv with 1 degree spatial resolution and 8 day temporal  
437 resolution.

#### 438 **2.4.4 ILAMB**

439 We used the International Land Model Benchmarking (ILAMB, v2.6) package for  
440 model assessment (Collier et al., 2018) focusing on global patterns of GPP (generated  
441 by Artificial Neural Networks and forced with CRUNCEPv6 meteorological data and  
442 MODIS; this reference GPP data was different from the one mentioned above, and the  
443 GPP is labeled as “GPP.ANN.CRUNCEPv6” Tramontana et al., 2016; Jung et al., 2017)  
444 and FLUXNET2015 (Pastorello et al., 2020). To distinguish this product from the one  
445 used above, we labeled it as MPI RS+METEO GPP. We also compared CliMA GPP to  
446 that from eight Coupled Model Intercomparison Project (CMIP) version 5 models and  
447 twelve CMIP version 6 models (Table S1).

448 We benchmarked the ILAMB overall score for the absolute values, as well as the  
449 individual components: the spatially integrated bias score, the root-mean-squared error  
450 (RMSE) score (doubly weighted in the overall score to emphasize its importance), the  
451 phase shift score, the inter-annual variability score, and the spatial distribution score.  
452 For the complete set of equations of each score and further details refer to Collier et al.  
453 (2018).

### 454 **3 Results**

#### 455 **3.1 Seasonal cycles**

456 CliMA Land simulated the characteristic seasonal cycles of carbon and water  
457 fluxes, and canopy reflectance and fluorescence (Figure 2). In general, the simulated SIF  
458 and NIRv tracked the simulated variations of GPP well for the eight selected grids with  
459 flux towers located within, except for some drought spells (e.g., days 150–350 in Figure  
460 2b; Marengo et al., 2021), as SIF and NIRv are less sensitive to the environmental stress  
461 than GPP (Magney et al., 2020; Marrs et al., 2020). We refer the readers to (Y. Wang,  
462 Braghieri, & Frankenberh, 2021) for videos of the hourly CliMA GPP, SIF, and NIRv for  
463 the year 2019.

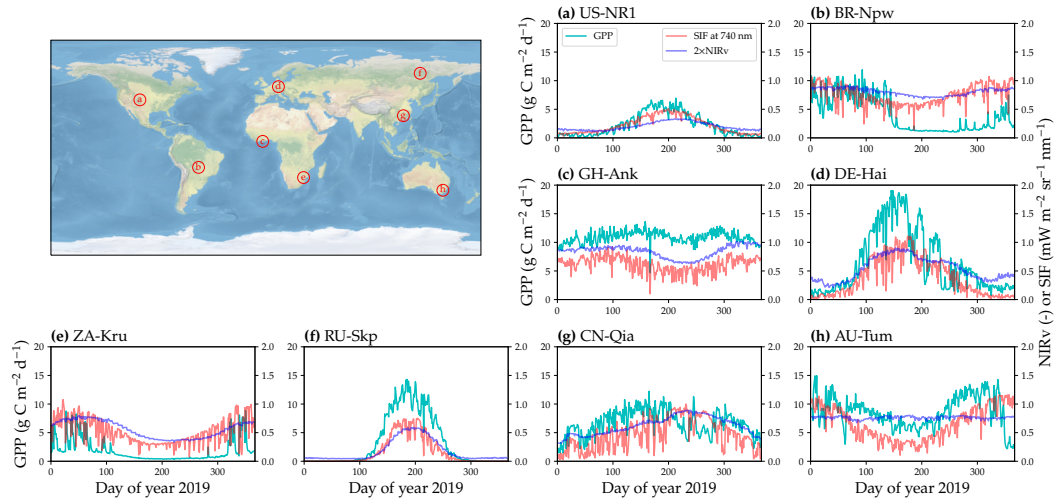


**Figure 2.** Example of CliMA Land run at eight sites across the globe. CliMA Land global run was made for year 2019. The [latitude, longitude] centers are (a) [40.5, -105.5], (b) [-16.5, -56.5], (c) [5.5, -2.5], (d) [51.5, 10.5], (e) [-25.5, 31.5], (f) [62.5, 129.5], (g) [26.5, 115.5], and (h) [-35.5, 148.5], respectively. There is a flux tower within each example grid, and they are US-NR1, BR-Npw, GH-Ank, DE-Hai, ZA-Kru, RU-Skp, CN-Qia, and AU-Tum, respectively. The cyan curve plots the modeled daily cumulative gross primary productivity (GPP); the red curve plots the modeled daily mean solar-induced chlorophyll fluorescence (SIF) at 740 nm; the blue curve plots the modeled daytime mean near infrared reflectance of vegetation (NIRv). NIRv is scaled to 2 times the original value to facilitate visualization. GPP, SIF, and NIRv are all daily means (nighttime values set to 0 for GPP and SIF).

464

### 3.2 GPP

465

466

467

468

469

470

471

CliMA GPP displayed reasonable spatial patterns across the globe: reproducing the patterns of MPI GPP which was interpolated from flux tower estimates (Figure 3). CliMA GPP and MPI GPP differed in their magnitudes (Figure 3), and CliMA annual mean GPP, on average, was higher than that of MPI GPP by about 63% ( $y = 1.629x + 0.024$  and  $R^2 = 0.806$  for the linear regression in Figure 3; slope significantly different from 1,  $p < 0.001$ ). The CliMA Land predicted a global GPP of 160.0 Pg C year<sup>-1</sup>, whereas the reference MPI GPP was 126.8 Pg C year<sup>-1</sup>.

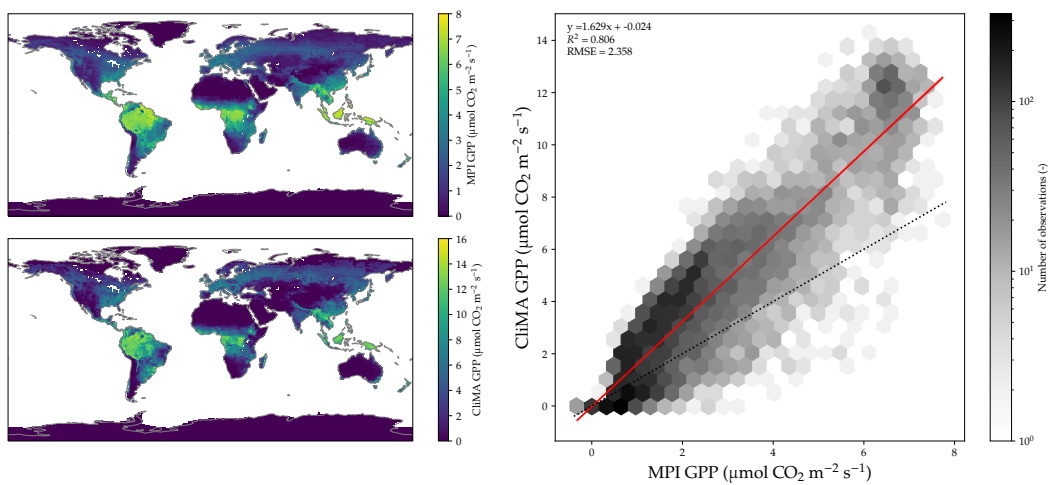


**Figure 3.** Comparison of gross primary productivity (GPP). CliMA Land global run was made for the year 2019. MPI GPP was interpolated from flux tower estimates using machine learning. GPP was annual means averaged from monthly averages (nighttime values set to 0). Red solid line with shaded region plots the linear regression with confidence intervals, and black dotted line plots the 1:1 line.

472

### 3.3 SIF

473

474

475

476

477

CliMA SIF<sub>683</sub> agreed well with observed spatial patterns of TROPOMI SIF<sub>683</sub>, though the two differed in their magnitude (Figure 4). CliMA SIF<sub>683</sub> was generally higher than TROPOMI SIF<sub>683</sub> given the negative TROPOMI SIF<sub>683</sub> values (Figure 4). The regression slope was close to 1 ( $y = 1.074x + 0.054$  and  $R^2 = 0.492$ ; slope significantly different from 1,  $p < 0.001$ ).

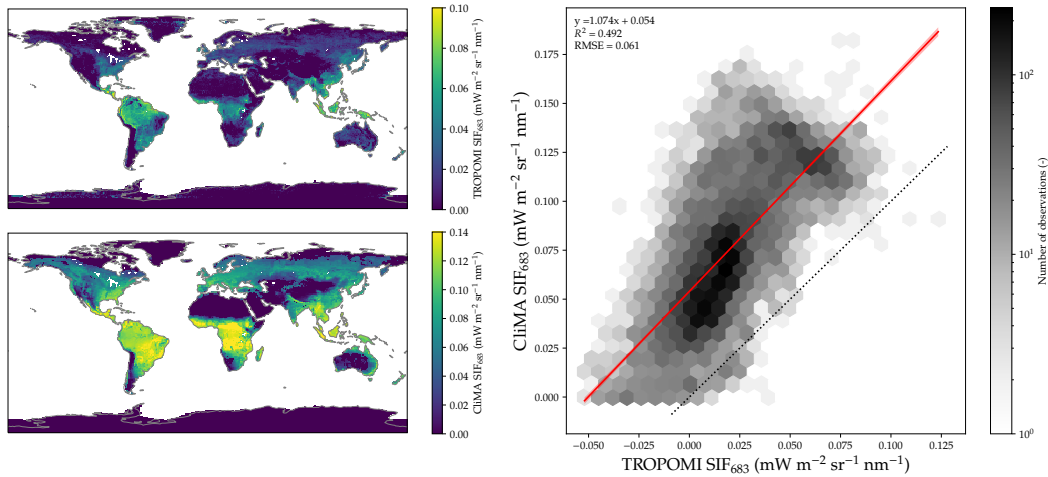


**Figure 4.** Comparison of solar induced chlorophyll fluorescence at 683 nm ( $SIF_{683}$ ). CliMA Land global run was made for the year 2019. TROPOMI  $SIF_{683}$  was regridded from satellite retrievals.  $SIF_{683}$  was annual means averaged from monthly averages (nighttime values set to 0). Red solid line with shaded region plots the linear regression with confidence intervals, and black dotted line plots the 1:1 line.

478 Similarly, CliMA  $SIF_{740}$  also well matched the spatial patterns of TROPOMI  
 479  $SIF_{740}$ , though the two also differed in their magnitudes (Figure 5). Slope of the  
 480 regression between the two was close to 1 ( $y = 1.263x + 0.118$  and  $R^2 = 0.495$ ; slope  
 481 significantly different from 1,  $p < 0.001$ ).

482 When compared to OCO-2  $SIF_{757}$ , while CliMA  $SIF_{757}$  well represented the  
 483 spatial patterns, it predicted dramatically higher  $SIF_{757}$  than OCO-2 retrievals  
 484 ( $y = 1.946x + 0.044$  and  $R^2 = 0.681$ ; slope significantly different from 1,  $p < 0.001$ ; Figure  
 485 6). The dramatically different magnitudes suggested potential issue in CliMA Land SIF  
 486 model or OCO-2  $SIF_{757}$  retrieval algorithm.

487 For SIF at 771 nm, CliMA  $SIF_{771}$  also well tracked the spatial patterns of OCO-2  
 488  $SIF_{771}$ , and the magnitude differed less than that for  $SIF_{757}$  ( $y = 1.392 + 0.039$  and  
 489  $R^2 = 0.633$ ; Figure 7). Though the slope was close to 1, it was still significantly different  
 490 from 1 ( $P < 0.001$ ).

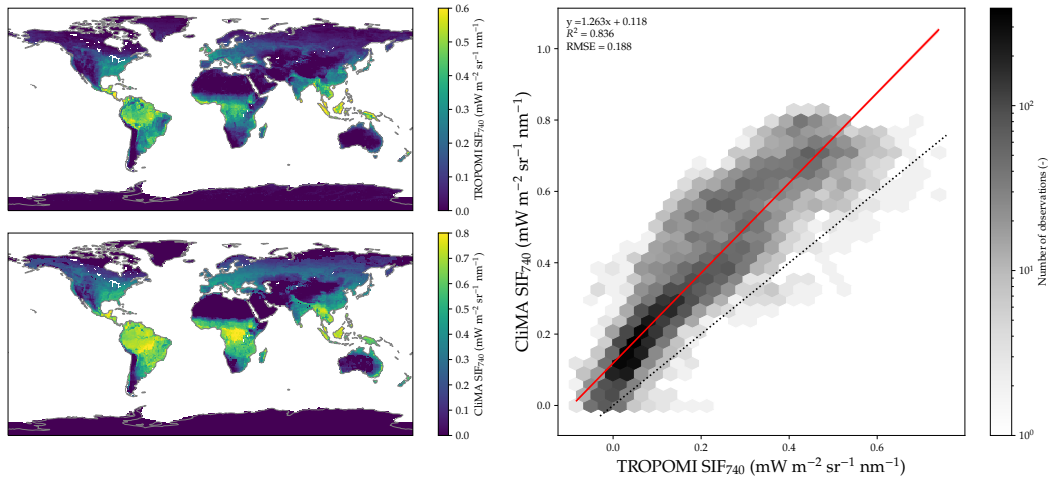


**Figure 5.** Comparison of solar induced chlorophyll fluorescence at 740 nm ( $SIF_{740}$ ). CliMA Land global run was made for the year 2019. TROPOMI  $SIF_{740}$  was regridded from satellite retrievals.  $SIF_{740}$  was annual means averaged from monthly averages (nighttime values set to 0). Red solid line with shaded region plots the linear regression with confidence intervals, and black dotted line plots the 1:1 line.

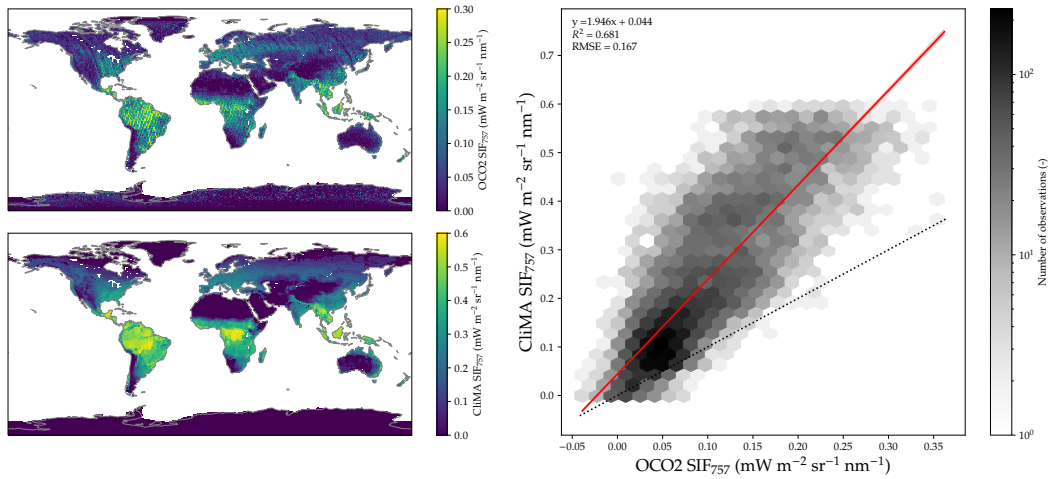


**Figure 6.** Comparison of solar induced chlorophyll fluorescence at 757 nm ( $SIF_{757}$ ). CliMA Land global run was made for the year 2019. OCO-2  $SIF_{757}$  was regridded from satellite retrievals.  $SIF_{757}$  was annual means averaged from monthly averages (nighttime values set to 0). Red solid line with shaded region plots the linear regression with confidence intervals, and black dotted line plots the 1:1 line.

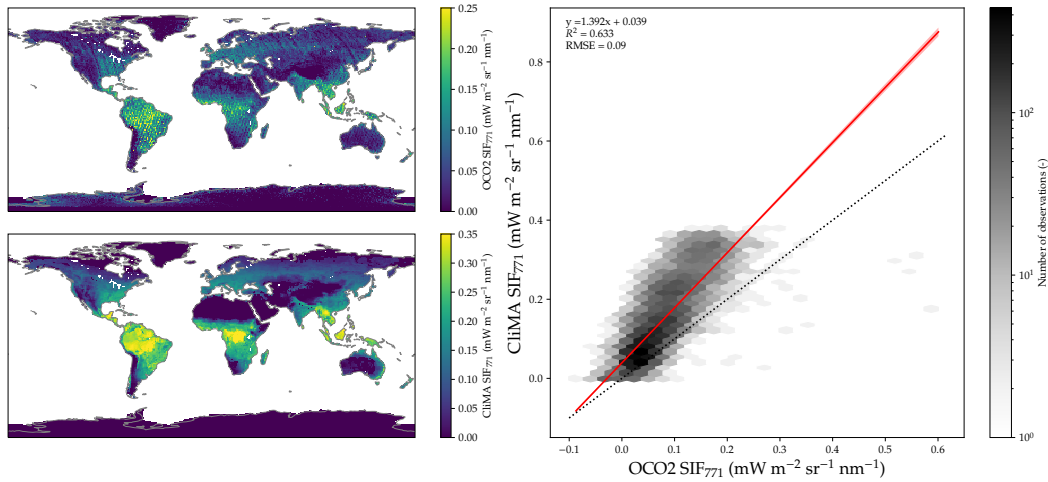


**Figure 7.** Comparison of solar induced chlorophyll fluorescence at 771 nm ( $SIF_{771}$ ). CliMA Land global run was made for the year 2019. OCO-2  $SIF_{771}$  was regridded from satellite retrievals.  $SIF_{771}$  was annual means averaged from monthly averages (nighttime values set to 0). Red solid line with shaded region plots the linear regression with confidence intervals, and black dotted line plots the 1:1 line.

#### 491 3.4 NDVI

492 CliMA NDVI (average daytime values) well reproduced the pattern of MODIS  
 493 NDVI (Figure 8). However, the two differed in their magnitude as CliMA NDVI was  
 494 generally higher than MODIS NDVI by 0.1 ( $y = 1.057x + 0.097$  and  $R^2 = 0.915$ ; slope  
 495 significantly different from 1; Figure 8).

#### 496 3.5 EVI

497 Similar to the comparison with MODIS NDVI, CliMA EVI (average daytime  
 498 values) also showed good agreement with MODIS EVI ( $y = 1.372x + 0.067$  and  
 499  $R^2 = 0.914$ ; slope significantly different from 1,  $p < 0.001$ ; Figure 9).

#### 500 3.6 NIRv

501 CliMA NIRv (average daytime values) well represented the spatial patterns  
 502 observed from MODIS NIRv, but the two differed in their magnitudes  
 503 ( $y = 1.691x - 0.010$  and  $R^2 = 0.875$ ; slope significantly different from 1,  $p < 0.001$ ; Figure  
 504 10).

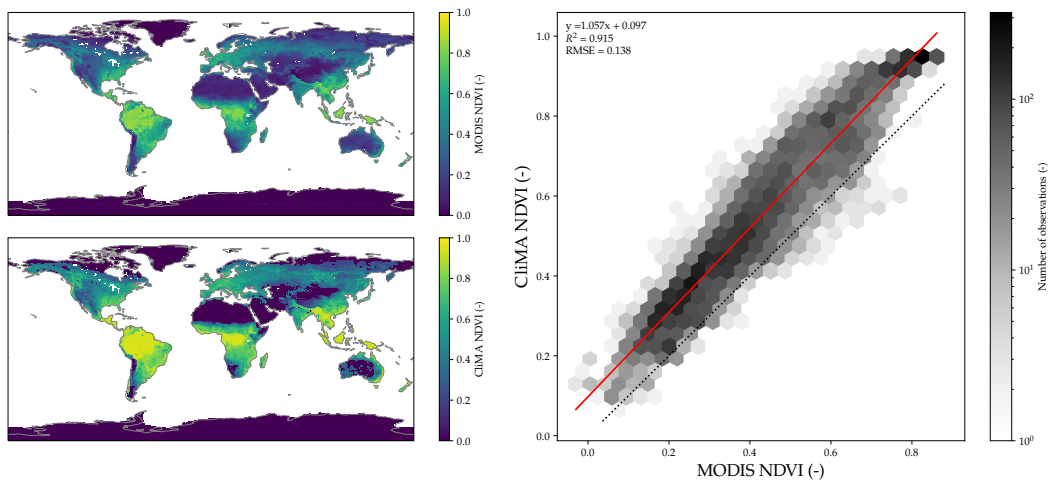


**Figure 8.** Comparison of normalized difference vegetation index (NDVI). CliMA Land global run was made for the year 2019. MODIS NDVI was regridded from satellite retrievals. NDVI was annual means averaged from 8-day averages (averaged from daytime values only). Red solid line with shaded region plots the linear regression with confidence intervals, and black dotted line plots the 1:1 line.

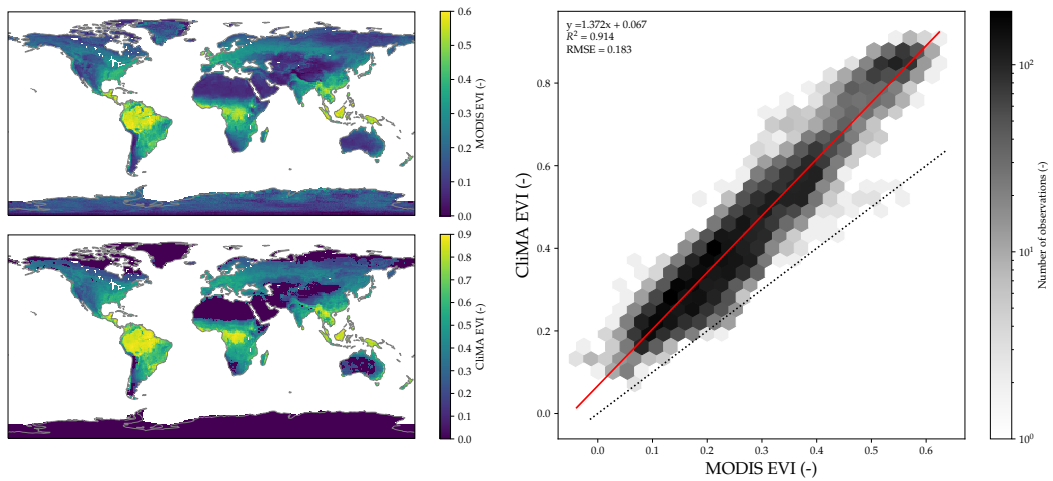


**Figure 9.** Comparison of enhanced vegetation index (EVI). CliMA Land global run was made for the year 2019. MODIS EVI was regridded from satellite retrievals. EVI was annual means averaged from 8-day averages (averaged from daytime values only). Red solid line with shaded region plots the linear regression with confidence intervals, and black dotted line plots the 1:1 line.

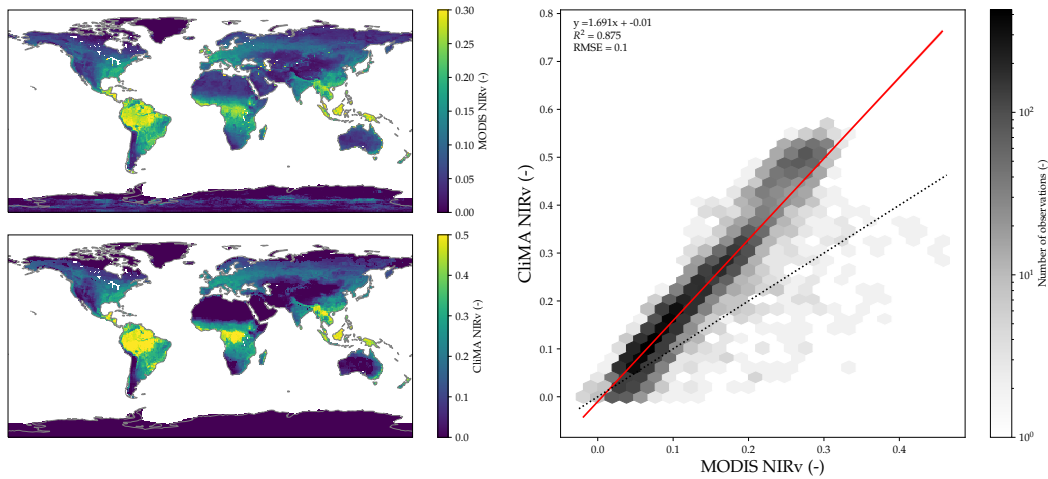


**Figure 10.** Comparison of near infrared reflectance of vegetation (NIRv). CliMA Land global run was made for the year 2019. MODIS NIRv was regridded from satellite retrievals. NIRv was annual means averaged from 8-day averages (averaged from daytime values only). Red solid line with shaded region plots the linear regression with confidence intervals, and black dotted line plots the 1:1 line.

### 3.7 ILAMB

The ILAMB results showed that CliMA Land had higher discrepancies with the reference estimate (MPI RS+METEO GPP) than the Ensemble CMIP5 (from 8 models) and the Ensemble CMIP6 (from 12 models). The discrepancies were larger both in terms of bias score and root-mean-square-error (RSME) in GPP, as CliMA Land predicted approximately 34% higher GPP than MPI RS+METEO GPP (CliMA Land GPP was  $155.1 \text{ Pg C year}^{-1}$  and MPI RS+METRO GPP was  $115.7 \text{ Pg C year}^{-1}$  for the year 2010). In terms of seasonal cycle score of GPP, CliMA Land performed similarly to Ensemble CMIP6, both of which showed better agreement with MPI RS+METEO GPP than the Ensemble CMIP5. Overall, CliMA Land was less closer to MPI RS+METEO GPP than Ensemble CMIP5 and CMIP6 in GPP given the higher CliMA GPP than MPI RS+METEO GPP. See Y. Wang, Braghieri, and Frankenberh (2021) for the complete set of ILAMB results (also available at [https://braghieri.github.io/ILAMB\\_CliMA\\_gpp\\_et/index.html](https://braghieri.github.io/ILAMB_CliMA_gpp_et/index.html)). We note that CliMA Land input parameters have not yet been calibrated to match field- or satellite-based measurements, and future calibrations will improve the model predictive

521 skills. It is also worth noting that MPI RS+METEO GPP is also an estimate of GPP and  
522 thus has significant uncertainty.

#### 523 **4 Discussion**

524 We present and evaluate CliMA Land, the first LSM that can simultaneously  
525 simulate hyperspectral canopy fluorescence and reflectance properties as well as  
526 corresponded carbon and water fluxes. CliMA Land modeled indices and measures, in  
527 general, well captured the spatial patterns globally, though the magnitude differed in  
528 some regions. These inconsistencies between model outputs and data-driven estimates  
529 potentially resulted from the following aspects, improvements over which would  
530 advance future land modeling.

531 (i) CliMA Land is not well constrained given the various sources of plant traits  
532 and environmental cues. First, the model input datasets often disagree in their  
533 assumptions and model complexity, likely resulting in biases in simulated results (see  
534 Y. Wang and Frankenberg (2021) for an example of how canopy model complexity  
535 impacts the simulated carbon, water, and fluorescence fluxes). Second, because of the  
536 limited knowledge of how plant physiological traits vary spatially and temporally,  
537 datasets used to drive CliMA Land are often temporally constant instead of a time  
538 series. For instance, photosynthetic capacity represented by  $V_{\text{cmax}25}$ , which should be  
539 varying in a growing season, is constant in a grid in our simulation, and this might  
540 contribute biases in the simulated carbon and water fluxes (Y. P. Wang et al., 2007).  
541 Third, CliMA Land prescribed environmental cues from ERA5 reanalysis data, which  
542 were interpolated from sparsely distributed historical observations and could have high  
543 uncertainty; and mismatch between ERA5 reanalysis data and reality would also  
544 contribute to biases in our model output. For example, when comparing the soil water  
545 contents from ERA5 reanalysis (black curve in Figure S1) vs. that from flux tower  
546 measurements (red curve with shaded region in Figure S1), we found that ERA5  
547 reanalysis data had wetter soil throughout the year, particularly from day 1 to 150,  
548 which corresponded to the growing season at AU-Tum. Promisingly, with the  
549 increasing number of observations across the globe, the uncertainty and biases  
550 resulting from model parameterization will be better resolved in the future (Cocchi et  
551 al., 2020).

552 (ii) Some key processes have been missing in the global-scale LSMs, such as the  
553 dynamics and variations in leaf photosynthesis and fluorescence related physiology.  
554 For example, Magney et al. (2019) and Raczka et al. (2019) highlighted the importance  
555 of sustained non-photochemical quenching (NPQ) in modeling SIF in the cold winter,  
556 which results in lower modeled SIF in cold environments. However, this process has  
557 not been yet implemented in any land surface or vegetation model (including CliMA  
558 Land) because of the lack of knowledge on how sustained NPQ quantitatively and  
559 mechanistically responds to temperature. Also, we used constant parameter sets for  
560 rate coefficient calculations such as the temperature dependency of maximum  
561 carboxylation rate, whereas species- and temperature-dependent parameter sets  
562 (Medlyn et al., 2002) should be used to best describe plants' acclimation to the  
563 environment. Similarly, the fluorescence parameter set we used to compute NPQ,  
564 fluorescence yield, and hence SIF (see van der Tol et al. (2014) for more details), was  
565 also constant across the globe, regardless of the site-level species composition and  
566 stress status. Future research efforts to implement new physiological processes and  
567 resolve the spatial and temporal variations and acclimation of these physiological  
568 parameters will also improve the predictive skills of LSMs.

569 (iii) The global scale data-driven GPP estimation used in the present study was  
570 interpolated using machine learning based on algorithm rather than real observations  
571 at  $1^\circ \times 1^\circ$  resolution, and thus had high uncertainty in the grids without a flux tower.  
572 Further, even for those grids with flux towers, there could be issues when up scaling  
573 flux tower observations that typically covers  $< 1 \text{ km}^2$  footprint to the entire grid that  
574 may range up to  $> 10000 \text{ km}^2$  and consist various vegetation types. A recent study  
575 compared 45 global GPP products and found considerable difference among the  
576 products, and the annual GPP ranges from approximately 0.8 to 2.4 times the MPI GPP  
577 (Zhang & Ye, 2021). In comparison, CliMA GPP was 1.26 times the MPI GPP for the  
578 year 2019. Therefore, as true global GPP patterns are unknown and current estimates  
579 are highly inconsistent (Anav et al., 2015; Zhang & Ye, 2021), effective evaluation of  
580 CliMA GPP or any other GPP remains a challenge.

581 (iv) The global-scale TROPOMI, OCO-2, and MODIS observations may have  
582 considerable errors. For example, the retrievals are often negative or close to zero,  
583 particularly in those regions with low vegetation cover, making it difficult for a 1:1  
584 comparison between CliMA Land output and satellite observations. As a result, there

585 is always a positive offset in the linear regressions. For example, SIF retrieval may use  
586 barren land as a baseline, and the potential illuminance from other chemicals other  
587 than chlorophyll could lead to biases over the baseline (Köhler et al., 2021). Moreover,  
588 the mismatch in sun-sensor geometry likely impacted the 1:1 comparison between  
589 CliMA Land and TROPOMI/OCO-2 SIF as we used a nadir viewing zenith angle for  
590 the global simulation. We note that the daily average SIF in CliMA Land was  
591 calculated by averaging the SIF at nadir throughout the diurnal cycle, whereas  
592 TROPOMI/OCO-2 daily mean SIF was converted from point measurements with  
593 varying solar zenith angles based on an assumption that SIF is a function of cosine  
594 solar zenith angle that peaks at midday, which may not be true. We note that CliMA  
595 Land allows for using specific sun-sensor geometry and solar time that match all  
596 satellite overpasses, enabling the direct comparison between model simulation and  
597 satellite retrievals rather than the averages (as done in Figure 16 of Y. Wang, Köhler, et  
598 al., 2021). As CliMA Land is equipped to utilize the data from multiple sources, such  
599 as flux tower and satellite observations, it allows for more systematic and  
600 comprehensive data assimilation, thus promoting future research on plant trait  
601 inversion at various spatial and temporal resolutions.

602 We note that CliMA predictions (pure forward model run without parameter  
603 calibration) were generally higher than existing MPI, TROPOMI, OCO-2, and MODIS  
604 products. Aside from errors in the reference benchmark datasets, the differences  
605 probably resulted from non-idealized model parameterization, such as chlorophyll  
606 content which was not inverted to use with a hyperspectral and multi-layer canopy RT  
607 model (so did many other input parameters). For example, if we use a lower  
608 chlorophyll content in the model, the vegetation will be less greener and thus NDVI,  
609 EVI, and NIRv will be lower; SIF and GPP will also be lower given the lower PAR  
610 absorption. Being able to simultaneously model hyperspectral canopy RT as well as  
611 carbon and water fluxes, CliMA Land has great potential in advancing future Earth  
612 System modeling. The simulated hyperspectral canopy RT can be directly compared to  
613 satellite observations, and can help constrain the Earth system model with the large  
614 number of remote sensing data such as inverting chlorophyll content that (1) is  
615 compatible with hyperspectral and multi-layer canopy RT model, and (2) agrees with  
616 remote sensing and/or ground-based data from multiple sources.

617 Further, the high temporal resolution of CliMA Land outputs provides an  
618 improved way to interpolate observations using modeled patterns (compared to  
619 prescribed constant trends such as when computing daily average SIF). The hourly  
620 global scales simulations allow for novel research that was not feasible in the past, such  
621 as the decoupling of SIF and NIRv vs. GPP in a diurnal cycle under different  
622 environmental stresses, supplementing the deficits of traditional satellite retrievals. We  
623 believe that future global maps with improved temporal resolutions (e.g., the NASA  
624 Surface Biology and Geology mission) can be used as model inputs, and that the  
625 implementation of new features into the land model will advance the land model  
626 predictive skills, for not only the past but also the future climate with respect to global  
627 climate change.

## 628 **5 Conclusions**

629 We present our first global run of CliMA Land, the first global land surface  
630 model that outputs carbon and water fluxes as well as hyperspectral canopy reflectance  
631 and fluorescence simultaneously. CliMA Land allows for not only the comparison of  
632 spatial patterns between carbon and water fluxes, reflectance, and chlorophyll  
633 fluorescence, but also provides insight into the details of their diurnal and seasonal  
634 cycles. We compare the model outputs to other data-driven GPP, SIF, NDVI, EVI, and  
635 NIRv products, and demonstrate the predictive skills of CliMA Land. Our model  
636 simulations underline (i) the necessity of improving land model parameterization, both  
637 spatially and temporally; (ii) the importance of implementing advanced or new features  
638 in the land surface models, such as the photosynthesis and fluorescence physiology;  
639 and (iii) the demand of integrating datasets to calibrate land surface models.

## 640 **Acknowledgements**

641 We gratefully acknowledge the generous support of Eric and Wendy Schmidt (by  
642 recommendation of the Schmidt Futures) and the Heising-Simons Foundation. This  
643 research has been supported by the National Aeronautics and Space Administration  
644 (NASA) Earth Sciences Division grant NNX15AH95G and NASA Carbon Cycle Science  
645 grant 80NSSC21K1712 awarded to Christian Frankenberg. M.L. was supported by the  
646 NASA Postdoctoral Program, administered by Universities Space Research Association  
647 under contract with NASA, and by the Next Generation Ecosystem

648 Experiments-Tropics, funded by the U.S. Department of Energy, Office of Science, Office  
649 of Biological and Environmental Research. Part of this research was carried out at the  
650 Jet Propulsion Laboratory, California Institute of Technology, under a contract with  
651 NASA. California Institute of Technology. Government sponsorship acknowledged. ©  
652 2021. All rights reserved. ERA5 data were generated using Copernicus Climate Change  
653 Service Information. Neither the European Commission nor the European Centre for  
654 Medium-Range Weather Forecasts (ECMWF) are responsible for any use that may be  
655 made of the Copernicus information or data in this publication. We gratefully thank  
656 Dr. Butler, Croft, Dai, He, Lawrence, Luo, Simard, Yamazaka, and Yuan for sharing the  
657 gridded datasets.

658 **References**

- 659 Anav, A., Friedlingstein, P., Beer, C., Ciais, P., Harper, A., Jones, C., . . . Zhao, M. (2015).  
 660 Spatiotemporal patterns of terrestrial gross primary production: A review. *Reviews*  
 661 *of Geophysics*, 53(3), 785–818.
- 662 Anav, A., Friedlingstein, P., Kidston, M., Bopp, L., Ciais, P., Cox, P., . . . Zhu, Z. (2013).  
 663 Evaluating the land and ocean components of the global carbon cycle in the CMIP5  
 664 earth system models. *Journal of Climate*, 26(18), 6801–6843.
- 665 Anderegg, W. R., Wolf, A., Arango-Velez, A., Choat, B., Chmura, D. J., Jansen, S., . . .  
 666 Pacala, S. (2018). Woody plants optimise stomatal behaviour relative to hydraulic  
 667 risk. *Ecology Letters*, 21(7), 968–977.
- 668 Anderegg, W. R. L., Schwalm, C., Biondi, F., Camarero, J. J., Koch, G., Litvak, M., . . .  
 669 Pacala, S. (2015). Pervasive drought legacies in forest ecosystems and their  
 670 implications for carbon cycle models. *Science*, 349(6247), 528–532.
- 671 Arora, V. K., Boer, G. J., Friedlingstein, P., Eby, M., Jones, C. D., Christian, J. R., . . . Wu, T.  
 672 (2013). Carbon–concentration and carbon–climate feedbacks in CMIP5 earth system  
 673 models. *Journal of Climate*, 26(15), 5289–5314.
- 674 Badgley, G., Anderegg, L. D., Berry, J. A., & Field, C. B. (2019). Terrestrial gross primary  
 675 production: Using nirv to scale from site to globe. *Global change biology*, 25(11),  
 676 3731–3740.
- 677 Badgley, G., Field, C. B., & Berry, J. A. (2017). Canopy near-infrared reflectance and  
 678 terrestrial photosynthesis. *Science advances*, 3(3), e1602244.
- 679 Baldocchi, D. D. (2020). How eddy covariance flux measurements have contributed to our  
 680 understanding of global change biology. *Global change biology*, 26(1), 242–260.
- 681 Baldocchi, D. D., Falge, E., Gu, L., Olson, R., Hollinger, D., Running, S., . . . Wofsy, S.  
 682 (2001). FLUXNET: A new tool to study the temporal and spatial variability of  
 683 ecosystem-scale carbon dioxide, water vapor, and energy flux densities. *Bulletin of*  
 684 *the American Meteorological Society*, 82(11), 2415–2434.
- 685 Ball, J. T., Woodrow, I. E., & Berry, J. A. (1987). A model predicting stomatal conductance  
 686 and its contribution to the control of photosynthesis under different environmental  
 687 conditions. In *Progress in photosynthesis research* (pp. 221–224). Springer.
- 688 Bonan, G. B., Patton, E. G., Finnigan, J. J., Baldocchi, D. D., & Harman, I. N. (2021).  
 689 Moving beyond the incorrect but useful paradigm: reevaluating big-leaf and  
 690 multilayer plant canopies to model biosphere-atmosphere fluxes—a review.

- 691 *Agricultural and Forest Meteorology*, 306, 108435.
- 692 Bonan, G. B., Patton, E. G., Harman, I. N., Oleson, K. W., Finnigan, J. J., Lu, Y., &  
 693 Burakowski, E. A. (2018). Modeling canopy-induced turbulence in the earth system:  
 694 A unified parameterization of turbulent exchange within plant canopies and the  
 695 roughness sublayer (clm-ml v0). *Geoscientific Model Development*, 11(4), 1467–1496.
- 696 Braghieri, R. K., Quaife, T., Black, E., He, L., & Chen, J. (2019). Underestimation of global  
 697 photosynthesis in earth system models due to representation of vegetation  
 698 structure. *Global Biogeochemical Cycles*, 33(11), 1358–1369.
- 699 Braghieri, R. K., Quaife, T., Black, E., Ryu, Y., Chen, Q., De Kauwe, M. G., & Baldocchi, D.  
 700 (2020). Influence of sun zenith angle on canopy clumping and the resulting impacts  
 701 on photosynthesis. *Agricultural and Forest Meteorology*, 291, 108065.
- 702 Braghieri, R. K., Wang, Y., Doughty, R., Sousa, D., Magney, T., Widlowski, J.-L., . . .  
 703 Frankenberg, C. (2021). Accounting for canopy structure improves hyperspectral  
 704 radiative transfer and sun-induced chlorophyll fluorescence representations in a  
 705 new generation earth system model. *Remote Sensing of Environment*, 261, 112497.
- 706 Butler, E. E., Datta, A., Flores-Moreno, H., Chen, M., Wythers, K. R., Fazayeli, F., . . . Reich,  
 707 P. B. (2017). Mapping local and global variability in plant trait distributions.  
 708 *Proceedings of the National Academy of Sciences*, 114(51), E10937–E10946.
- 709 Campbell, G. S., & Norman, J. M. (1998). *An introduction to environmental biophysics*.  
 710 Springer Science & Business Media, New York, New York, USA.
- 711 Collier, N., Hoffman, F. M., Lawrence, D. M., Keppel-Aleks, G., Koven, C. D., Riley, W. J.,  
 712 . . . Randerson, J. T. (2018). The international land model benchmarking (ilamb)  
 713 system: design, theory, and implementation. *Journal of Advances in Modeling Earth  
 714 Systems*, 10(11), 2731–2754.
- 715 Croft, H., Chen, J., Wang, R., Mo, G., Luo, S., Luo, X., . . . Bonal, D. (2020). The global  
 716 distribution of leaf chlorophyll content. *Remote Sensing of Environment*, 236, 111479.
- 717 Cucchi, M., Weedon, G. P., Amici, A., Bellouin, N., Lange, S., Müller Schmied, H., . . .  
 718 Buontempo, C. (2020). Wfde5: bias-adjusted era5 reanalysis data for impact studies.  
 719 *Earth System Science Data*, 12(3), 2097–2120.
- 720 Dai, Y., Xin, Q., Wei, N., Zhang, Y., Shangguan, W., Yuan, H., . . . Lu, X. (2019). A global  
 721 high-resolution data set of soil hydraulic and thermal properties for land surface  
 722 modeling. *Journal of Advances in Modeling Earth Systems*, 11(9), 2996–3023.
- 723 De Kauwe, M. G., Kala, J., Lin, Y.-S., Pitman, A. J., Medlyn, B. E., Duursma, R. A., . . .

- 724 Miralles, D. G. (2015). A test of an optimal stomatal conductance scheme within the  
 725 cable land surface model. *Geoscientific Model Development*, 8(2), 431–452.
- 726 Doughty, R., Xiao, X., Köhler, P., Frankenberg, C., Qin, Y., Wu, X., . . . Moore III, B. (2021).  
 727 Global-scale consistency of spaceborne vegetation indices, chlorophyll fluorescence,  
 728 and photosynthesis. *Journal of Geophysical Research: Biogeosciences*, e2020JG006136.
- 729 Eller, C. B., Rowland, L., Oliveira, R. S., Bittencourt, P. R. L., Barros, F. V., da Costa,  
 730 A. C. L., . . . Cox, P. (2018). Modelling tropical forest responses to drought and El  
 731 Niño with a stomatal optimization model based on xylem hydraulics. *Philosophical  
 732 Transactions of the Royal Society B: Biological Sciences*, 373(1760), 20170315.
- 733 Frankenberg, C., Fisher, J. B., Worden, J., Badgley, G., Saatchi, S. S., Lee, J.-E., . . . Yokota, T.  
 734 (2011). New global observations of the terrestrial carbon cycle from gosat: Patterns  
 735 of plant fluorescence with gross primary productivity. *Geophysical Research Letters*,  
 736 38(17).
- 737 He, L., Chen, J. M., Pisek, J., Schaaf, C. B., & Strahler, A. H. (2012). Global clumping index  
 738 map derived from the modis brdf product. *Remote Sensing of Environment*, 119,  
 739 118–130.
- 740 Helm, L. T., Shi, H., Lerda, M. T., & Yang, X. (2020). Solar-induced chlorophyll  
 741 fluorescence and short-term photosynthetic response to drought. *Ecological  
 742 Applications*, 30(5), e02101.
- 743 Hersbach, H., Bell, B., Berrisford, P., Biavati, G., Horányi, A., Muñoz Sabater, J., . . .  
 744 Thépaut, J.-N. (2018). Era5 hourly data on single levels from 1979 to present.  
 745 *Copernicus Climate Change Service (C3S) Climate Data Store (CDS)*, (Accessed on  
 746 04-Aug-2021), 10.24381/cds.adbb2d47.
- 747 Hersbach, H., Bell, B., Berrisford, P., Hirahara, S., Horányi, A., Muñoz-Sabater, J., . . .  
 748 Thépaut, J.-N. (2020). The ERA5 global reanalysis. *Quarterly Journal of the Royal  
 749 Meteorological Society*, 146(730), 1999–2049.
- 750 Jiang, C., & Fang, H. (2019). Gsv: a general model for hyperspectral soil reflectance  
 751 simulation. *International Journal of Applied Earth Observation and Geoinformation*, 83,  
 752 101932.
- 753 Jones, C., Robertson, E., Arora, V., Friedlingstein, P., Shevliakova, E., Bopp, L., . . . Tjiputra,  
 754 J. (2013). Twenty-first-century compatible CO<sub>2</sub> emissions and airborne fraction  
 755 simulated by CMIP5 earth system models under four representative concentration  
 756 pathways. *Journal of Climate*, 26(13), 4398–4413.

- 757 Jung, M., Reichstein, M., Margolis, H. A., Cescatti, A., Richardson, A. D., Arain, M. A., . . .  
 758 Williams, C. (2011). Global patterns of land-atmosphere fluxes of carbon dioxide,  
 759 latent heat, and sensible heat derived from eddy covariance, satellite, and  
 760 meteorological observations. *Journal of Geophysical Research: Biogeosciences*, 116(G3).
- 761 Jung, M., Reichstein, M., Schwalm, C. R., Huntingford, C., Sitch, S., Ahlström, A., . . .  
 762 Zeng, N. (2017). Compensatory water effects link yearly global land CO<sub>2</sub> sink  
 763 changes to temperature. *Nature*, 541(7638), 516–520.
- 764 Jung, M., Schwalm, C., Migliavacca, M., Walther, S., Camps-Valls, G., Koirala, S., . . .  
 765 Reichstein, M. (2020). Scaling carbon fluxes from eddy covariance sites to globe:  
 766 synthesis and evaluation of the fluxcom approach. *Biogeosciences*, 17(5), 1343–1365.
- 767 Kennedy, D., Swenson, S., Oleson, K. W., Lawrence, D. M., Fisher, R., Lola da Costa, A. C.,  
 768 & Gentile, P. (2019). Implementing plant hydraulics in the community land model,  
 769 version 5. *Journal of Advances in Modeling Earth Systems*, 11(2), 485–513.
- 770 Köhler, P., Fischer, W. W., Rossman, G. R., Grotzinger, J. P., Doughty, R., Wang, Y., . . .  
 771 Frankenberg, C. (2021). Mineral luminescence observed from space. *Geophysical*  
 772 *Research Letters*, 48(19), e2021GL095227.
- 773 Köhler, P., Frankenberg, C., Magney, T. S., Guanter, L., Joiner, J., & Landgraf, J. (2018).  
 774 Global retrievals of solar-induced chlorophyll fluorescence with TROPOMI: First  
 775 results and intersensor comparison to OCO-2. *Geophysical Research Letters*, 45(19),  
 776 10,456–10,463.
- 777 Konings, A. G., Saatchi, S. S., Frankenberg, C., Keller, M., Leshyk, V., Anderegg, W. R., . . .  
 778 Zuidema, P. A. (2021). Detecting forest response to droughts with global  
 779 observations of vegetation water content. *Global change biology*, 27(23), 6005–6024.
- 780 Lawrence, D. M., Fisher, R. A., Koven, C. D., Oleson, K. W., Swenson, S. C., Bonan, G., . . .  
 781 Zeng, X. (2019). The community land model version 5: Description of new features,  
 782 benchmarking, and impact of forcing uncertainty. *Journal of Advances in Modeling*  
 783 *Earth Systems*, 11(12), 4245–4287.
- 784 Lawrence, P. J., & Chase, T. N. (2007). Representing a new modis consistent land surface  
 785 in the community land model (clm 3.0). *Journal of Geophysical Research:*  
 786 *Biogeosciences*, 112, G01023.
- 787 Le Quéré, C., Andrew, R. M., Friedlingstein, P., Sitch, S., Pongratz, J., Manning, A. C., . . .  
 788 Zhu, D. (2018). Global carbon budget 2017. *Earth System Science Data*, 10(1), 405–448.

789

- 790 Leuning, R. (1995). A critical appraisal of a combined stomatal-photosynthesis model for  
791  $C_3$  plants. *Plant, Cell & Environment*, 18(4), 339–355.
- 792 Luo, X., Keenan, T. F., Chen, J. M., Croft, H., Colin Prentice, I., Smith, N. G., . . . Zhang, Y.  
793 (2021). Global variation in the fraction of leaf nitrogen allocated to photosynthesis.  
794 *Nature Communications*, 12(1), 4866.
- 795 Magney, T. S., Barnes, M. L., & Yang, X. (2020). On the covariation of chlorophyll  
796 fluorescence and photosynthesis across scales. *Geophysical Research Letters*, 47(23),  
797 e2020GL091098.
- 798 Magney, T. S., Bowling, D. R., Logan, B. A., Grossmann, K., Stutz, J., Blanken, P. D., . . .  
799 Frankenberg, C. (2019). Mechanistic evidence for tracking the seasonality of  
800 photosynthesis with solar-induced fluorescence. *Proceedings of the National Academy  
801 of Sciences*, 116(24), 11640–11645.
- 802 Marengo, J. A., Cunha, A. P., Cuartas, L. A., Deusdará Leal, K. R., Broedel, E., Seluchi,  
803 M. E., . . . Bender, F. (2021). Extreme drought in the brazilian pantanal in 2019–2020:  
804 Characterization, causes, and impacts. *Frontiers in Water*, 3, 13.
- 805 Marrs, J., Reblin, J., Logan, B., Allen, D., Reinmann, A., Bombard, D., . . . Hutrya, L.  
806 (2020). Solar-induced fluorescence does not track photosynthetic carbon  
807 assimilation following induced stomatal closure. *Geophysical Research Letters*, 47(15),  
808 e2020GL087956.
- 809 Medlyn, B. E., Dreyer, E., Ellsworth, D., Forstreuter, M., Harley, P. C., Kirschbaum,  
810 M. U. F., . . . Loustau, D. (2002). Temperature response of parameters of a  
811 biochemically based model of photosynthesis. II. A review of experimental data.  
812 *Plant, Cell & Environment*, 25(9), 1167–1179.
- 813 Medlyn, B. E., Duursma, R. A., Eamus, D., Ellsworth, D. S., Prentice, I. C., Barton,  
814 C. V. M., . . . Wingate, L. (2011). Reconciling the optimal and empirical approaches  
815 to modelling stomatal conductance. *Global Change Biology*, 17(6), 2134–2144.
- 816 Medlyn, B. E., Duursma, R. A., & Zeppel, M. J. (2011). Forest productivity under climate  
817 change: a checklist for evaluating model studies. *Wiley Interdisciplinary Reviews:  
818 Climate Change*, 2(3), 332–355.
- 819 Norby, R. J., Gu, L., Haworth, I. C., Jensen, A. M., Turner, B. L., Walker, A. P., . . . Winter,  
820 K. (2017). Informing models through empirical relationships between foliar  
821 phosphorus, nitrogen and photosynthesis across diverse woody species in tropical  
822 forests of panama. *New Phytologist*, 215(4), 1425–1437.

- 823 Norton, A. J., Rayner, P. J., Koffi, E. N., & Scholze, M. (2018). Assimilating solar-induced  
824 chlorophyll fluorescence into the terrestrial biosphere model bethy-scope v1.0:  
825 model description and information content. *Geoscientific Model Development*, *11*(4),  
826 1517–1536.
- 827 Norton, A. J., Rayner, P. J., Koffi, E. N., Scholze, M., Silver, J. D., & Wang, Y.-P. (2019).  
828 Estimating global gross primary productivity using chlorophyll fluorescence and a  
829 data assimilation system with the bethy-scope model. *Biogeosciences*, *16*(15),  
830 3069–3093.
- 831 Pastorello, G., Trotta, C., Canfora, E., Chu, H., Christianson, D., Cheah, Y.-W., . . . Papale,  
832 D. (2020). The FLUXNET2015 dataset and the ONEFlux processing pipeline for  
833 eddy covariance data. *Scientific Data*, *7*(1), 225.
- 834 Pinty, B., Lavergne, T., Dickinson, R., Widlowski, J.-L., Gobron, N., & Verstraete, M.  
835 (2006). Simplifying the interaction of land surfaces with radiation for relating  
836 remote sensing products to climate models. *Journal of Geophysical Research:*  
837 *Atmospheres*, *111*(D2).
- 838 Powell, T. L., Galbraith, D. R., Christoffersen, B. O., Harper, A., Imbuzeiro, H., Rowland,  
839 L., . . . Moorcroft, P. R. (2013). Confronting model predictions of carbon fluxes with  
840 measurements of Amazon forests subjected to experimental drought. *New*  
841 *Phytologist*, *200*(2), 350–365.
- 842 Qiu, B., Chen, J. M., Ju, W., Zhang, Q., & Zhang, Y. (2019). Simulating emission and  
843 scattering of solar-induced chlorophyll fluorescence at far-red band in global  
844 vegetation with different canopy structures. *Remote Sensing of Environment*, *233*,  
845 111373.
- 846 Raczka, B., Porcar-Castell, A., Magney, T., Lee, J. E., Köhler, P., Frankenberg, C., . . .  
847 Bowling, D. R. (2019). Sustained nonphotochemical quenching shapes the seasonal  
848 pattern of solar-induced fluorescence at a high-elevation evergreen forest. *Journal of*  
849 *Geophysical Research: Biogeosciences*, *124*(7), 2005–2020.
- 850 Reid, R. C., Prausnitz, J. M., & Poling, B. E. (1987). *The properties of gases and liquids*.  
851 McGraw Hill Book Co., New York, NY.
- 852 Schaaf, C., & Wang, Z. (2015). *Mcd43a4 modis/terra+aqua brdf/albedo nadir brdf adjusted ref*  
853 *daily l3 global - 500m v006*. NASA EOSDIS Land Processes DAAC. Retrieved from  
854 <https://lpdaac.usgs.gov/products/mcd43a4v006> doi:  
855 10.5067/MODIS/MCD43A4.006

- 856 Schimel, D., Pavlick, R., Fisher, J. B., Asner, G. P., Saatchi, S., Townsend, P., . . . Cox, P.  
857 (2015). Observing terrestrial ecosystems and the carbon cycle from space. *Global*  
858 *Change Biology*, 21(5), 1762–1776.
- 859 Schimel, D., Schneider, F. D., Carbon, J., & Participants, E. (2019). Flux towers in the sky:  
860 global ecology from space. *New Phytologist*, 224(2), 570–584.
- 861 Shiklomanov, A. N., Dietze, M. C., Fer, I., Viskari, T., & Serbin, S. P. (2021). Cutting out the  
862 middleman: calibrating and validating a dynamic vegetation model (ed2-prospect5)  
863 using remotely sensed surface reflectance. *Geoscientific Model Development*, 14(5),  
864 2603–2633.
- 865 Simard, M., Pinto, N., Fisher, J. B., & Baccini, A. (2011). Mapping forest canopy height  
866 globally with spaceborne lidar. *Journal of Geophysical Research: Biogeosciences*,  
867 116(G4021).
- 868 Sperry, J. S., & Love, D. M. (2015). What plant hydraulics can tell us about responses to  
869 climate-change droughts. *New Phytologist*, 207(1), 14–27.
- 870 Sperry, J. S., Venturas, M. D., Anderegg, W. R. L., Mencuccini, M., Mackay, D. S., Wang, Y.,  
871 & Love, D. M. (2017). Predicting stomatal responses to the environment from the  
872 optimization of photosynthetic gain and hydraulic cost. *Plant, Cell & Environment*,  
873 40(6), 816–830.
- 874 Sperry, J. S., Venturas, M. D., Todd, H. N., Trugman, A. T., Anderegg, W. R. L., Wang, Y.,  
875 & Tai, X. (2019). The impact of rising CO<sub>2</sub> and acclimation on the response of US  
876 forests to global warming. *Proceedings of the National Academy of Sciences*, 116(51),  
877 25734–25744.
- 878 Sperry, J. S., Wang, Y., Wolfe, B. T., Mackay, D. S., Anderegg, W. R. L., McDowell, N. G., &  
879 Pockman, W. T. (2016). Pragmatic hydraulic theory predicts stomatal responses to  
880 climatic water deficits. *New Phytologist*, 212(3), 577–589.
- 881 Sun, Y., Frankenberg, C., Jung, M., Joiner, J., Guanter, L., Köhler, P., & Magney, T. (2018).  
882 Overview of Solar-Induced chlorophyll Fluorescence (SIF) from the Orbiting Carbon  
883 Observatory-2: Retrieval, cross-mission comparison, and global monitoring for GPP.  
884 *Remote Sensing of Environment*, 209, 808–823.
- 885 Sun, Y., Frankenberg, C., Wood, J. D., Schimel, D., Jung, M., Guanter, L., . . . others (2017).  
886 Oco-2 advances photosynthesis observation from space via solar-induced  
887 chlorophyll fluorescence. *Science*, 358(6360).
- 888 Tramontana, G., Jung, M., Schwalm, C. R., Ichii, K., Camps-Valls, G., Ráduly, B., . . .

- 889 Papale, D. (2016). Predicting carbon dioxide and energy fluxes across global fluxnet  
890 sites with regression algorithms. *Biogeosciences*, 13(14), 4291–4313.
- 891 Trugman, A. T., Medvigy, D., Mankin, J. S., & Anderegg, W. R. L. (2018). Soil moisture  
892 stress as a major driver of carbon cycle uncertainty. *Geophysical Research Letters*,  
893 45(13), 6495–6503.
- 894 van der Tol, C., Berry, J., Campbell, P., & Rascher, U. (2014). Models of fluorescence and  
895 photosynthesis for interpreting measurements of solar-induced chlorophyll  
896 fluorescence. *Journal of Geophysical Research: Biogeosciences*, 119(12), 2312–2327.
- 897 van der Tol, C., Verhoef, W., Timmermans, J., Verhoef, A., & Su, Z. (2009). An integrated  
898 model of soil-canopy spectral radiances, photosynthesis, fluorescence, temperature  
899 and energy balance. *Biogeosciences*, 6(12).
- 900 van Genuchten, M. T. (1980). A closed-form equation for predicting the hydraulic  
901 conductivity of unsaturated soils. *Soil science society of America journal*, 44(5),  
902 892–898.
- 903 Venturas, M. D., Sperry, J. S., Love, D. M., Frehner, E. H., Allred, M. G., Wang, Y., &  
904 Anderegg, W. R. L. (2018). A stomatal control model based on optimization of  
905 carbon gain versus hydraulic risk predicts aspen sapling responses to drought. *New*  
906 *Phytologist*, 220(3), 836–850.
- 907 Walker, A. P., Beckerman, A. P., Gu, L., Kattge, J., Cernusak, L. A., Domingues, T. F., . . .  
908 Woodward, F. I. (2014). The relationship of leaf photosynthetic traits— $V_{\text{cmax}}$  and  
909  $J_{\text{max}}$ —to leaf nitrogen, leaf phosphorus, and specific leaf area: A meta-analysis and  
910 modeling study. *Ecology and Evolution*, 4(16), 3218–3235.
- 911 Wang, Y., Anderegg, W. R., Venturas, M. D., Trugman, A. T., Yu, K., & Frankenberg, C.  
912 (2021). Optimization theory explains nighttime stomatal responses. *New Phytologist*,  
913 230(4), 1550–1561.
- 914 Wang, Y., Braghieri, R. K., & Frankenberg, C. (2021). *Global scale carbon and water fluxes*  
915 *and canopy spectra simulation using the clima land (v0.1)*. CaltechDATA. Retrieved  
916 from <https://data.caltech.edu/records/2191> doi: 10.22002/D1.2191
- 917 Wang, Y., & Frankenberg, C. (2021). On the impact of canopy model complexity on  
918 simulated carbon, water, and solar-induced chlorophyll fluorescence fluxes.  
919 *Biogeosciences Discussions*, 2021, 1–23. doi: 10.5194/bg-2021-214
- 920 Wang, Y., Köhler, P., He, L., Doughty, R., Braghieri, R. K., Wood, J. D., & Frankenberg, C.  
921 (2021). Testing stomatal models at the stand level in deciduous angiosperm and

- 922 evergreen gymnosperm forests using clima land (v0.1). *Geoscientific Model*  
 923 *Development*, 14(11), 6741–6763.
- 924 Wang, Y., Sperry, J. S., Anderegg, W. R. L., Venturas, M. D., & Trugman, A. T. (2020). A  
 925 theoretical and empirical assessment of stomatal optimization modeling. *New*  
 926 *Phytologist*, 227, 311–325.
- 927 Wang, Y., Sperry, J. S., Venturas, M. D., Trugman, A. T., Love, D. M., & Anderegg, W. R. L.  
 928 (2019). The stomatal response to rising CO<sub>2</sub> concentration and drought is predicted  
 929 by a hydraulic trait-based optimization model. *Tree Physiology*, 39, 1416–1427.
- 930 Wang, Y. P., Baldocchi, D., Leuning, R., Falge, E., & Vesala, T. (2007). Estimating  
 931 parameters in a land-surface model by applying nonlinear inversion to eddy  
 932 covariance flux measurements from eight fluxnet sites. *Global Change Biology*, 13(3),  
 933 652–670.
- 934 Wehr, R., Munger, J., McManus, J., Nelson, D., Zahniser, M., Davidson, E., . . . Saleska, S.  
 935 (2016). Seasonality of temperate forest photosynthesis and daytime respiration.  
 936 *Nature*, 534(7609), 680–683.
- 937 Yamazaki, D., Ikeshima, D., Tawatari, R., Yamaguchi, T., O’Loughlin, F., Neal, J. C., . . .  
 938 Bates, P. D. (2017). A high-accuracy map of global terrain elevations. *Geophysical*  
 939 *Research Letters*, 44(11), 5844–5853.
- 940 Yang, P., Prikaziuk, E., Verhoef, W., & van der Tol, C. (2021). Scope 2.0: a model to  
 941 simulate vegetated land surface fluxes and satellite signals. *Geoscientific Model*  
 942 *Development*, 14(7), 4697–4712.
- 943 Yang, P., Verhoef, W., & van der Tol, C. (2017). The mscope model: A simple adaptation to  
 944 the scope model to describe reflectance, fluorescence and photosynthesis of  
 945 vertically heterogeneous canopies. *Remote sensing of environment*, 201, 1–11.
- 946 Yuan, H., Dai, Y., & Li, S. (2020). *Reprocessed MODIS version 6 leaf area index data sets for*  
 947 *land surface and climate modelling*. Sun Yat-sun University. Retrieved from  
 948 <http://globalchange.bnu.edu.cn/research/laiv6>
- 949 Yuan, H., Dai, Y., Xiao, Z., Ji, D., & Shangguan, W. (2011). Reprocessing the modis leaf  
 950 area index products for land surface and climate modelling. *Remote Sensing of*  
 951 *Environment*, 115(5), 1171–1187.
- 952 Zhang, Y., Guanter, L., Berry, J. A., van der Tol, C., Yang, X., Tang, J., & Zhang, F. (2016).  
 953 Model-based analysis of the relationship between sun-induced chlorophyll  
 954 fluorescence and gross primary production for remote sensing applications. *Remote*

955            *Sensing of Environment*, 187, 145–155.

956        Zhang, Y., Xiao, X., Wu, X., Zhou, S., Zhang, G., Qin, Y., & Dong, J. (2017). A global  
957            moderate resolution dataset of gross primary production of vegetation for  
958            2000–2016. *Scientific data*, 4, 170165.

959        Zhang, Y., & Ye, A. (2021). Would the obtainable gross primary productivity (gpp)  
960            products stand up? a critical assessment of 45 global gpp products. *Science of The*  
961            *Total Environment*, 783, 146965.

# **Supporting Information for “Modeling global carbon and water fluxes and hyperspectral canopy radiative transfer simultaneously using a next generation land surface model—CliMA Land”**

## **Contents of this file**

1. Note S1
2. Table S1
3. Figures S1

## **Introduction**

Note S1 describes the method we used to invert hyperspectral soil albedo from known broadband PAR and NIR albedo values.

Figures S1 and S2 plot the comparison of soil water time series from ERA5 reanalysis data and flux tower observations at AU-Tum (site h of Figure 2 in the main text).

**Note S1.** Hyperspectral soil albedo

Firstly, to derive hyperspectral soil albedo, we calculate soil albedo values at photosynthetically active radiation (PAR) region and near infrared (NIR) regions, denoted as  $\alpha_{\text{PAR}}$  and  $\alpha_{\text{NIR}}$  respectively, by linearly interpolating the reference values at completely wet and dry soils:

$$\alpha_{\text{PAR}} = \alpha_{\text{PAR,wet}} \cdot \text{RSWC} + \alpha_{\text{PAR,dry}} \cdot (1 - \text{RSWC}), \quad (1)$$

$$\alpha_{\text{NIR}} = \alpha_{\text{NIR,wet}} \cdot \text{RSWC} + \alpha_{\text{NIR,dry}} \cdot (1 - \text{RSWC}), \quad (2)$$

where RSWC is the relative volumetric soil water content (0 when completely dry, 1 when soil water content is saturated), the subscript “wet” denotes saturated soil, and the subscript “dry” denotes completely dry soil. The four reference albedo values at a RSWC = 0 and RSWC = 1 can be found in Community Land Model (Table 3.3 in CLM tech notes version 5). Our adapted method differs from the original CLM approach, which uses

$$\alpha_{\text{PAR}} = \max(\alpha_{\text{PAR,dry}}, \alpha_{\text{PAR,wet}} + 0.11 - 0.4 \cdot \text{SWC}),$$

$$\alpha_{\text{NIR}} = \max(\alpha_{\text{NIR,dry}}, \alpha_{\text{NIR,wet}} + 0.11 - 0.4 \cdot \text{SWC}),$$

where SWC is the absolute volumetric soil water content (0 when completely dry, < 1 when saturated). Our adapted soil albedo method linearly interpolates the soil albedo from wet to dry soil, and better matches experimental observations than the original CLM approach (Figure S1.1).

Secondly, we expand the broadband albedo values to hyperspectral by weighing the characteristic soil albedo bands:

$$\alpha(\lambda) = \sum_i f(i) \cdot A(i, \lambda), \quad (3)$$

where  $\alpha(\lambda)$  is the albedo at wavelength  $\lambda$ ,  $f(i)$  is the weight of the  $i$ th characteristic albedo band, and  $A(i, \lambda)$  is the  $i$ th characteristic albedo band. See Figure S1.2 for the four bands.

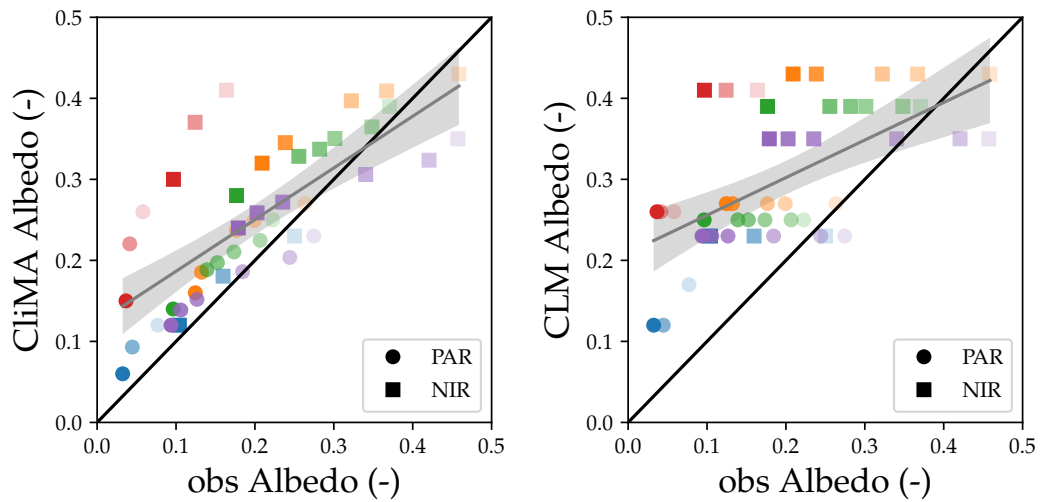


**Figure S1.1.** Comparison of the broadband albedo computed using the CliMA Land and CLM approach. Data from (Jiang & Fang, 2019).

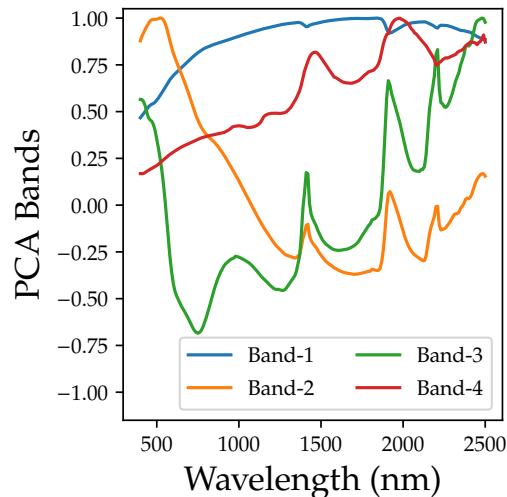


**Figure S1.2.** Characteristic soil albedo bands of the GSV model (Jiang & Fang, 2019).

We use six methods to fit the weights: three methods using only first two characteristic bands (two fitted weights) and three methods using all four characteristic bands (four fitted weights). Each of the categories contains (1) point method that fits averages, (2) curve method that fit curves, and (3) hybrid method that fits a point and a curve. The six methods are labeled as 2P, 2C, 2H, 4P, 4C, and 4H, respectively. The point method weighs the PAR and NIR region

equally, and minimizes the sum of the square error between the averages:

$$\min \left[ \left( \overline{\alpha_{\text{PAR,mod}}} - \alpha_{\text{PAR,ref}} \right)^2 + \left( \overline{\alpha_{\text{NIR,mod}}} - \alpha_{\text{NIR,ref}} \right)^2 \right]. \quad (4)$$

The curve method assumes the target is a two-piece flat curve that the PAR region is constant at  $\alpha_{\text{PAR,ref}}$  and the NIR region is constant at  $\alpha_{\text{NIR,ref}}$ , and minimizes the square error between modeled and target curves:

$$\min \left( \overline{\alpha_{\text{mod}}} - \alpha_{\text{ref}} \right)^2. \quad (5)$$

The hybrid method weighs the PAR and NIR regions equally, and minimizes the sum of (1) the square error between the averages in the PAR region and (2) square of mean absolute difference between modeled and target curve in the NIR region:

$$\min \left[ \left( \overline{\alpha_{\text{PAR,mod}}} - \alpha_{\text{PAR,ref}} \right)^2 + \left( \overline{|\alpha_{\text{NIR,mod}} - \alpha_{\text{NIR,ref}}|} \right)^2 \right]. \quad (6)$$

See Figure S1.3 for the examples of the fitting methods. Overall, 4H performs the best (Figure S1.4), and we use it in our CliMA Land simulations. Note here that method 4P fits 4 values from 2 albedo so that it does not converge. As a result, method 4P has extremely high error compared to others.

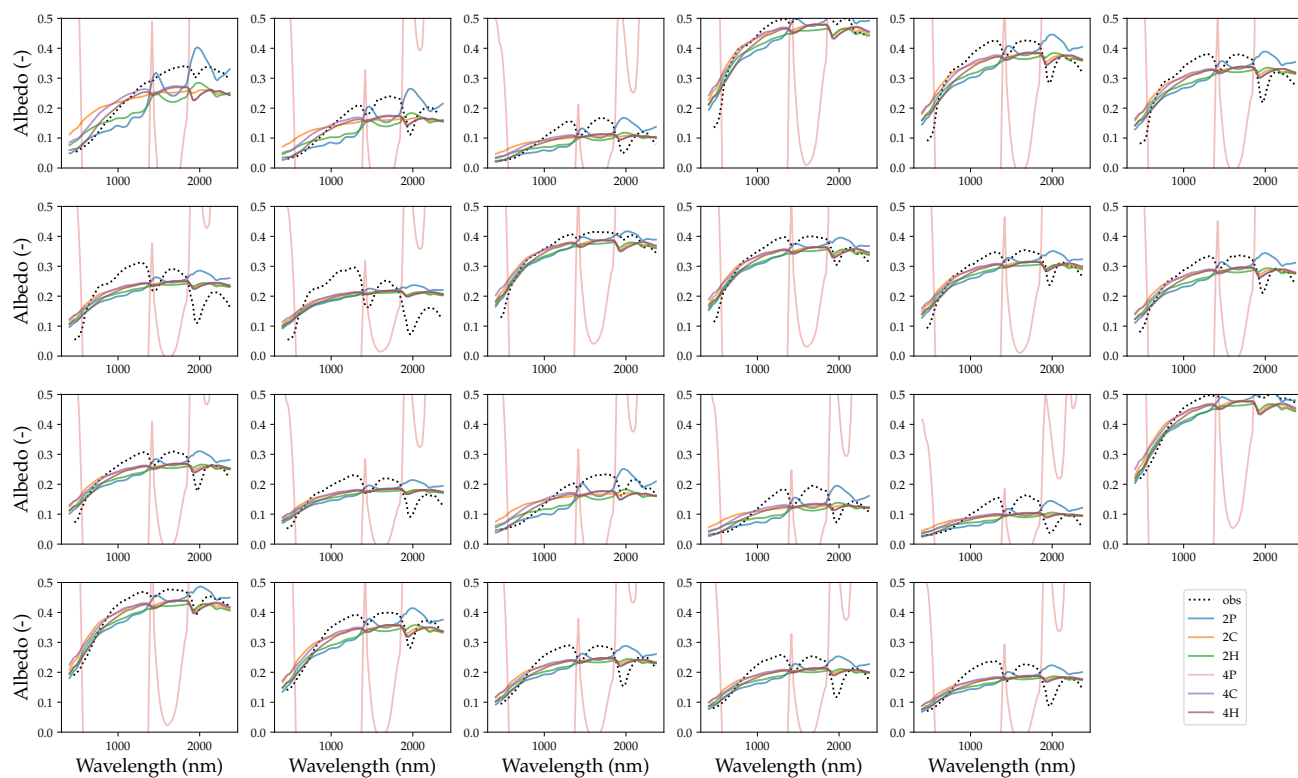


**Figure S1.3.** Examples of the performances of the six fitting methods. Data from (Jiang & Fang, 2019).

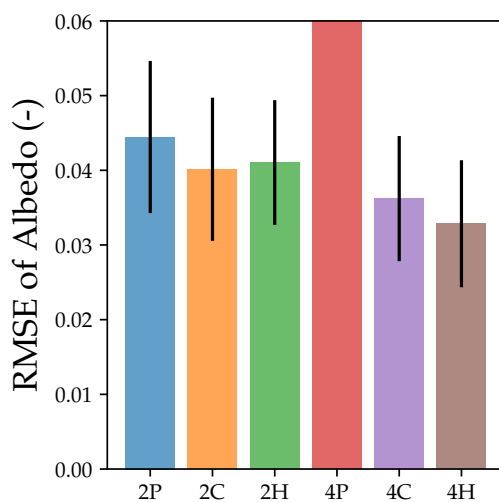


**Figure S1.4.** Performances of the six fitting methods. Data from (Jiang & Fang, 2019).

**Table S1.** Coupled Model Intercomparison Project (CMIP) models used for benchmarking.

CMIP5 Model	Reference	CMIP6 Model	Reference	
ACCESS1-3	(Lewis & Karoly, 2014)	ACCESS-ESM1-5	(Ziehn et al., 2019)	
CanESM2	(Chylek et al., 2011)	BCC-CSM2-MR	(Wu et al., 2018)	
		CanESM5	(Swart et al., 2019)	
		CESM2	(Danabasoglu, 2019)	
GFDL-ESM2M	(GFDL, 2014)	CNRM-ESM2-1	(Seferian, 2018)	
		GFDL-ESM4	(Horowitz et al., 2018)	
		GISS-E2-1-G	(NASA GISS, 2018)	
HadGEM2-CC	(Jones et al., 2011)	IPSL-CM6A-LR	(Boucher et al., 2018)	
IPSL-CM5A-LR	(Dufresne et al., 2013)			
MIROC-ESM	(Watanabe et al., 2011)		MIROC-ES2L	(Tachiiri et al., 2019)
MPI-ESM-LR	(Giorgetta et al., 2013)		MPI-ESM1-2-LR	(Wieners et al., 2019)
NorESM1-M	(NCC, 2011)		NorESM2-LM	(Seland et al., 2019)
			UKESM1-0-LL	(Tang et al., 2019)

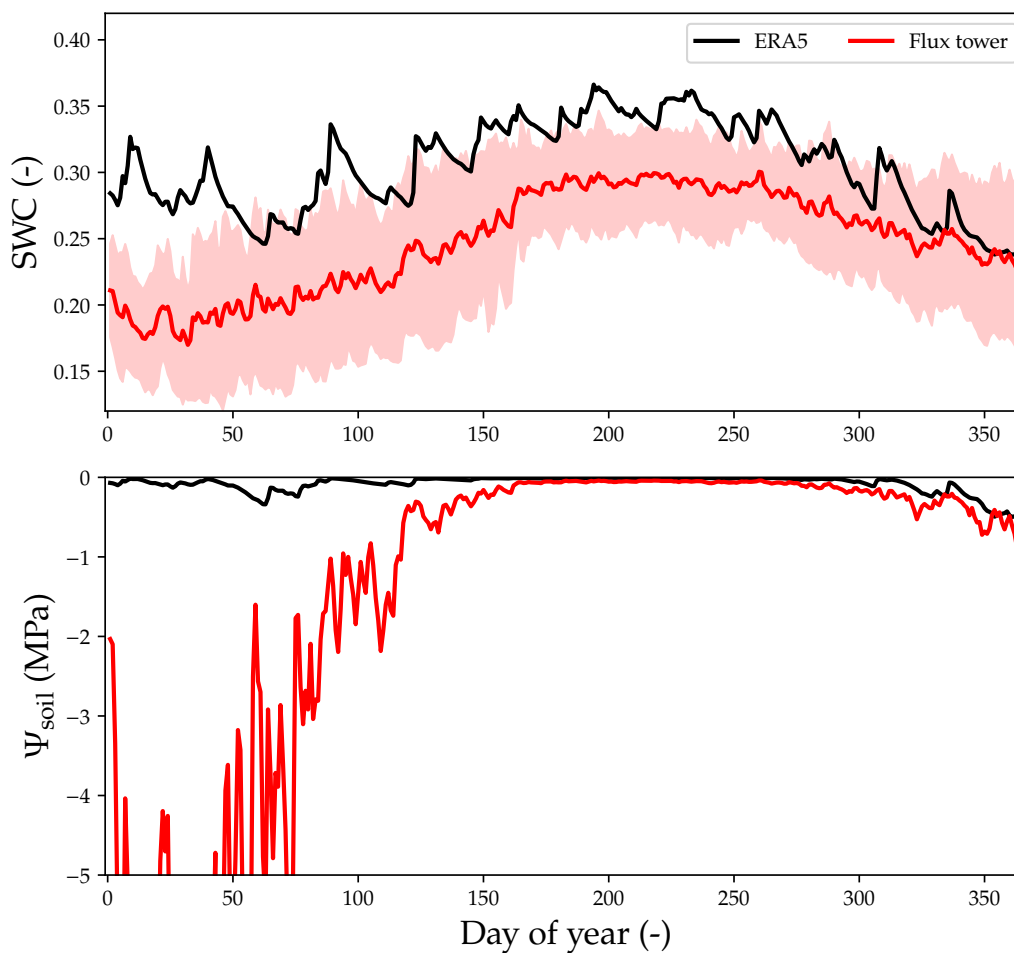


**Figure S1.** Comparison of soil water time series from ERA5 reanalysis data and flux tower observations at AU-Tum (site h of Figure 2 in the main text). Soil water content (SWC) from ERA5 is averaged from that of four soil layers (black curve), and SWC from flux tower is averaged from that of the same day from year 2001 to 2014 (shaded red region indicates the standard deviation, SD). Soil water potential ( $\Psi_{\text{soil}}$ ) is computed from corresponding SWC using the van Genuchten equation (van Genuchten, 1980) using the gridded soil hydraulic parameters from Dai et al. (2019) for the site. Red region plots the  $\Psi_{\text{soil}}$  with SWC in the range of mean  $\pm$  SD.

## References

- Boucher, O., Denvil, S., Levvasseur, G., Cozic, A., Caubel, A., Foujols, M.-A., . . . Cheruy, F. (2018). *Ipsl ipsl-cm6a-lr model output prepared for cmip6 cmip*. Earth System Grid Federation. doi: 10.22033/ESGF/CMIP6.1534
- Chylek, P., Li, J., Dubey, M., Wang, M., & Lesins, G. (2011). Observed and model simulated 20th century arctic temperature variability: Canadian earth system model canesm2. *Atmospheric Chemistry and Physics Discussions*, 11(8), 22893–22907.
- Dai, Y., Xin, Q., Wei, N., Zhang, Y., Shangguan, W., Yuan, H., . . . Lu, X. (2019). A global high-resolution data set of soil hydraulic and thermal properties for land surface modeling. *Journal of Advances in Modeling Earth Systems*, 11(9), 2996–3023.
- Danabasoglu, G. (2019). *Ncar cesm2 model output prepared for cmip6 cmip historical*. Earth System Grid Federation. doi: 10.22033/ESGF/CMIP6.7627
- Dufresne, J.-L., Foujols, M.-A., Denvil, S., Caubel, A., Marti, O., Aumont, O., . . . Vuichard, N. (2013). Climate change projections using the ipsl-cm5 earth system model: from cmip3 to cmip5. *Climate dynamics*, 40(9), 2123–2165.
- GFDL. (2014). *Noaa gfdl gfdl-esm2m, historicalmisc experiment output for cmip5 ar5, served by esgf*. World Data Center for Climate (WDCC) at DKRZ. doi: 10.1594/WDCC/CMIP5.NGEMhm
- Giorgetta, M. A., Jungclaus, J., Reick, C. H., Legutke, S., Bader, J., Böttinger, M., . . . Stevens, B. (2013). Climate and carbon cycle changes from 1850 to 2100 in mpi-esm simulations for the coupled model intercomparison project phase 5. *Journal of Advances in Modeling Earth Systems*, 5(3), 572–597.
- Horowitz, L. W., Naik, V., Sentman, L., Paulot, F., Blanton, C., McHugh, C., . . . Zeng, Y.

- (2018). *Noaa-gfdl gfdl-esm4 model output prepared for cmip6 aerchemmip*. Earth System Grid Federation. doi: 10.22033/ESGF/CMIP6.1404
- Jiang, C., & Fang, H. (2019). Gsv: a general model for hyperspectral soil reflectance simulation. *International Journal of Applied Earth Observation and Geoinformation*, 83, 101932.
- Jones, C. D., Hughes, J. K., Bellouin, N., Hardiman, S. C., Jones, G. S., Knight, J., . . . Zerroukat, M. (2011). The hadgem2-es implementation of cmip5 centennial simulations. *Geoscientific Model Development*, 4(3), 543–570.
- Lewis, S. C., & Karoly, D. J. (2014). Assessment of forced responses of the australian community climate and earth system simulator (access) 1.3 in cmip5 historical detection and attribution experiments. *AUSTRALIAN BUREAU METEOROLOGY*.
- NASA GISS. (2018). *Nasa-giss giss-e2.1g model output prepared for cmip6 ismip6*. Earth System Grid Federation. doi: 10.22033/ESGF/CMIP6.2066
- NCC. (2011). *Noresm1-m model output prepared for cmip5, served by esgf*. World Data Center for Climate (WDCC) at DKRZ.
- Seferian, R. (2018). *Cnrm-cerfacs cnrm-esm2-1 model output prepared for cmip6 cmip*. Earth System Grid Federation. doi: 10.22033/ESGF/CMIP6.1391
- Seland, Ø., Bentsen, M., Olivière, D. J. L., Toniazzo, T., Gjermundsen, A., Graff, L. S., . . . Schulz, M. (2019). *Ncc noresm2-lm model output prepared for cmip6 cmip historical*. Earth System Grid Federation. doi: 10.22033/ESGF/CMIP6.8036
- Swart, N. C., Cole, J. N., Kharin, V. V., Lazare, M., Scinocca, J. F., Gillett, N. P., . . . Sigmund, M. (2019). *Ccma canesm5 model output prepared for cmip6 scenariomip*. Earth System Grid Federation. doi: 10.22033/ESGF/CMIP6.1317
- Tachiiri, K., Abe, M., Hajima, T., Arakawa, O., Suzuki, T., Komuro, Y., . . . Kawamiya, M.

- (2019). *Miroc miroc-es2l model output prepared for cmip6 scenariomip*. Earth System Grid Federation. doi: 10.22033/ESGF/CMIP6.936
- Tang, Y., Rumbold, S., Ellis, R., Kelley, D., Mulcahy, J., Sellar, A., . . . Jones, C. (2019). *Mohc ukesm1.0-ll model output prepared for cmip6 cmip historical*. Earth System Grid Federation. doi: 10.22033/ESGF/CMIP6.6113
- van Genuchten, M. T. (1980). A closed-form equation for predicting the hydraulic conductivity of unsaturated soils. *Soil science society of America journal*, 44(5), 892–898.
- Watanabe, S., Hajima, T., Sudo, K., Nagashima, T., Takemura, T., Okajima, H., . . . Kawamiya, M. (2011). Miroc-esm 2010: model description and basic results of cmip5-20c3m experiments. *Geoscientific Model Development*, 4(4), 845–872.
- Wieners, K.-H., Giorgetta, M., Jungclaus, J., Reick, C., Esch, M., Bittner, M., . . . Roeckner, E. (2019). *Mpi-m mpi-esm1.2-lr model output prepared for cmip6 scenariomip ssp245*. Earth System Grid Federation. doi: 10.22033/ESGF/CMIP6.6693
- Wu, T., Chu, M., Dong, M., Fang, Y., Jie, W., Li, J., . . . Zhang, Y. (2018). *Bcc bcc-csm2mr model output prepared for cmip6 cmip picontrl*. Earth System Grid Federation. doi: 10.22033/ESGF/CMIP6.3016
- Ziehn, T., Chamberlain, M., Lenton, A., Law, R., Bodman, R., Dix, M., . . . Druken, K. (2019). *Csiro access-esm1.5 model output prepared for cmip6 cmip*. Earth System Grid Federation. doi: 10.22033/ESGF/CMIP6.2288